ZJU-AERO V0.5: An Accurate and Efficient Radar Operator Designed for CMA-GFS / MESO with Capability of Simulating Non-spherical Hydrometeors

Hejun Xie[1], Lei Bi[1], Wei Han[2,3]

5

[1]Key Laboratory of Geoscience Big Data and Deep Resource of Zhejiang Province, School of Earth Sciences, Zhejiang University, Hangzhou, 310027, China

[2]CMA Earth System Modeling and Prediction Centre (CEMC), China Meteorological Administration, Beijing 100081, China

10 [3]State Key Laboratory of Severe Weather (LaSW), Chinese Academy of Meteorological Sciences, China Meteorological Administration, Beijing, 100081, China

Correspondence to: Lei Bi (bilei@zju.edu.cn), Wei Han (hanwei@cma.gov.cn)

Abstract. In this study, we present a new forward polarimetric radar operator called the Accurate and Efficient Radar Operator designed by ZheJiang University (ZJU-AERO). This operator was designed to interface with the numerical weather prediction

15 (NWP) model of the global forecast system/regional mesoscale model of the China Meteorology Administration (CMA-GFS/MESO). The main objective of developing this observation operator was to assimilate observations from the Precipitation Measurement Radar (PMR) and ground-based radar's polarimetric radar variables, excluding the Doppler variables. To calculate the hydrometeor optical properties of ZJU-AERO, we utilized the invariant-imbedding T-matrix (IITM) method, which can handle non-spherical and inhomogeneous hydrometeor particles in the atmosphere. The optical database of ZJU-

20 AERO was designed with a multi-layered architecture to ensure the flexibility in hydrometeor morphology and orientation specifications, while maintaining operational efficiency. In this work, we elaborate on the design concepts, physical basis, and hydrometeor specifications of ZJU-AERO. Additionally, we present a case study demonstrating the application of ZJU-AERO in simulating radar observations of Typhoon Haishen.

1 Introduction

25 The development of regional models with finer horizontal resolutions, such as the Chinese operational regional numerical weather prediction (NWP) model, known as the regional mesoscale model of China Meteorology Administration (CMA-MESO) (Chen et al., 2008; Shen et al., 2023), necessitates the acquisition of more convective-scale information about the atmosphere to improve quantitative precipitation forecasts. Fortunately, the measurements from space-borne and ground-based weather radars provide valuable sources of three-dimensional kilometre-scale volume data with high temporal resolutions.

30 However, weather radar can only observe the amplitude and phase of electromagnetic waves echoed from meteorological

objects, specifically various types of hydrometeors. Except for the Doppler radar variables, such as radial velocity (beyond the scope of this study), it is challenging to establish a connection between the prognostic variables simulated by the NWP model and the observable polarimetric radar variables, which are inferred from the statistical moments of voltage time series collected by the receiver of the weather radar electronics system (Zhang, 2016).

35 The software package introduced in this work is referred to as a "forward radar operator", designed to transform the model prognostic variables into the observation space, resulting in equivalent simulated synthetic radar variables. Utilizing a unified forward radar operator for assimilations and retrievals is believed to be superior to employing an ensemble of retrieval relationships along with pre-processing procedures and corrections for different frequencies and platforms. In essence, using radar data in the observation space is preferred over the model space due to the highly non-linear and non-unique nature of

40 the observational operator of polarimetric radar.

Several radar operators have been developed and published over the past several decades. For instance, Jung et al. (2008) implemented a polarimetric radar simulator known as the Polarimetric Radar data Simulator developed by the Center for Analysis and Prediction of Storms (CAPS-PRS) at the University of Oklahoma. This simulator uses spheroids to characterize hydrometeors and computes optical properties using online Rayleigh approximations or offline look-up tables (LUT)

45 constructed by the extended boundary condition method (EBCM) described in Mishchenko and Travis (1994). This simulator has been applied to low-frequency bands, such as S-, C- and X-band. Ryzhkov et al. (2011) described another radar operator for research purposes, which is designed for spectra-resolving cloud microphysics models and is more computationally expensive. Zeng et al. (2016) described an efficient radar operator described for operational data assimilation purposes in the COSMO model, but it focuses on non-polarimetric radar variables. In addition to the above operators, Wolfensberger and

50 Berne (2018) reported a cross-platform polarimetric radar operator termed POLarimetric forward radar operator for the Consortium for Small-scale Modelling (COSMO) model (COSMO-POL). This operator was designed for the COSMO–NWP model and can simulate melting particles. The optical database of the COSMO-POL was constructed also by using the EBCM, characterizing all hydrometeor particles as homogeneous spheroids. However, in the COSMO-POL, the hydrometeor orientations and shape parameter settings are fixed at the level of the optical database, which limits sensitivity testing and fine-

55 tuning. Wang and Liu (2019) reported a forward reflectivity observation operator (together with its tangent linear and adjoint operator) with simulation capability of frozen hydrometeors designed for data assimilation purpose of ground-based radar in Weather Research & Forecasting Model (WRF), in which the simulated reflectivity are parameterized as fast polynomial-relationships with respect to mixing ratios of hydrometeors. More recently, Oue et al. (2020) developed the Cloud-resolving model Radar SIMulator (CR-SIM), which can simulate polarimetric Radar and light detection and ranging (Lidar) observations

60 for various Cloud Resolving Models (CRM), including the WRF, Icosahedral Nonhydrostatic Weather and Climate Model (ICON), Regional Atmospheric Modeling System (RAMS), and Advective Statistical Forecast Model (SAM). CRM-SIM has a unique capability of explicitly representing rimming procedure by coupling with the prognostic variable known as rimming ratio in the Predicted Particle Properties (P3) microphysics package (Morrison and Milbrandt, 2015). However, CR-SIM is currently limited to ground-based platforms and offers no explicit treatment for melting particles.

65   This work aimed to design a cross-band and cross-platform radar operator for research purposes, such as microphysics package validation, and operational data assimilation use in CMA–GFS / MESO. This radar operator features an accurate, multi-layered, and flexible optical database of non-spherical and inhomogeneous hydrometeor particles. The software prototype, called the Accurate and Efficient Radar Operator designed by ZheJiang University (ZJU-AERO), addresses the scattering computation of hydrometeors and construction of optical properties database as the key aspects in the evolution of the radar operator. This

70   software has also inherited established techniques, such as sub-beam sampling, used for simulating the effects of beam bending/broadening/shielding (Ryzhkov, 2007).

The development of ZJU-AERO was primarily motivated by the future data assimilation purpose of the precipitation measurement radar (PMR) onboard the FengYun-3 Rain Measurement satellite (FY3-RM). The parameters of the instrument FY3-RM/PMR are comparable with those of the Global Precipitation Measurement/Dual-Frequency Precipitation Radar

75   (GPM/DPR). The dual-frequency precipitation radar (DPR) onboard the GPM was designed to obtain the storm structure, rainfall rates, drop size distributions (DSD), path-integrated attenuation, and other useful information that are not available from passive sensor observations (Iguchi et al., 2003). Both PMR and DPR have two bands (the Ku- and Ka-bands), while PMR is designed with a swath of 303 km, horizontal resolution of 5 km at nadir, and radial resolution of 250 m.

Furthermore, the instrument, the Second Generation of Precipitation Radar (PR2), for RM constellation is presently undergoing

80   active research. It is an advanced version of PMR with the capability of dual-polarization and dual-bands. It has a side-scan mode that can transmit and receive beams with large zenith angles to observe polarimetric radar variables. Therefore, the polarimetric potential of ZJU-AERO would be useful in the future.

This study is organized into several sections. Section 2 provides readers with an overview of the general concepts of ZJU-AERO. The formulas relating bulk scattering properties to the observed radar variables are briefly presented here to clarify the

85   notation convention used in this study and eliminate ambiguity in the context. Details of the implementation of hydrometeor settings, including dielectric models, aspect ratio models, orientation preference models, and particle size distributions (PSDs) are also listed in Section 2. Section 3 elaborates on the flexible architecture of the state-of-the-art non-spherical scattering properties database, which distinguishes the ZJU-AERO from its predecessors. The characteristics of the multi-layered optical database are illustrated using a non-spheroid hydrometeor model, namely the Chebyshev-shaped raindrop. Moreover, Section

90   4 presents a case study of observations of a tropical cyclone given by the space-borne radar GPM/DPR, compared with simulations given by the ZJU-AERO. Sensitivity tests of PSDs and non-sphericity are also described in this section. Section 5 summarizes this study and describes the development plans for the ZJU-AERO.

2 General Descriptions of ZJU-AERO

95 The ZJU-AERO was developed to simulate the observable polarimetric radar variables for radar systems aboard on various platforms, including ground-based, space-borne, and potentially airborne radars in the future. While the physical principles of the weather radar detection process are universal, certain factors, such as beam-broadening, beam-bending, and beam-blocking among others (as shown in Figure 1), are not equally important across platforms. For example, the beam-bending effect is typically negligible for space-borne radar due to large absolute elevation angles (usually 70~90°) and shorter beam trajectories

100 (usually < 20 km) below the tropopause, as compared to the ground-based radar (the trajectory can reach up to about 250 km). However, the simulations of space-borne and ground-based radars share consistent hydrometeor setting entries, such as the dielectric model, particle morphology (distribution), size distribution, orientation preference, and others.
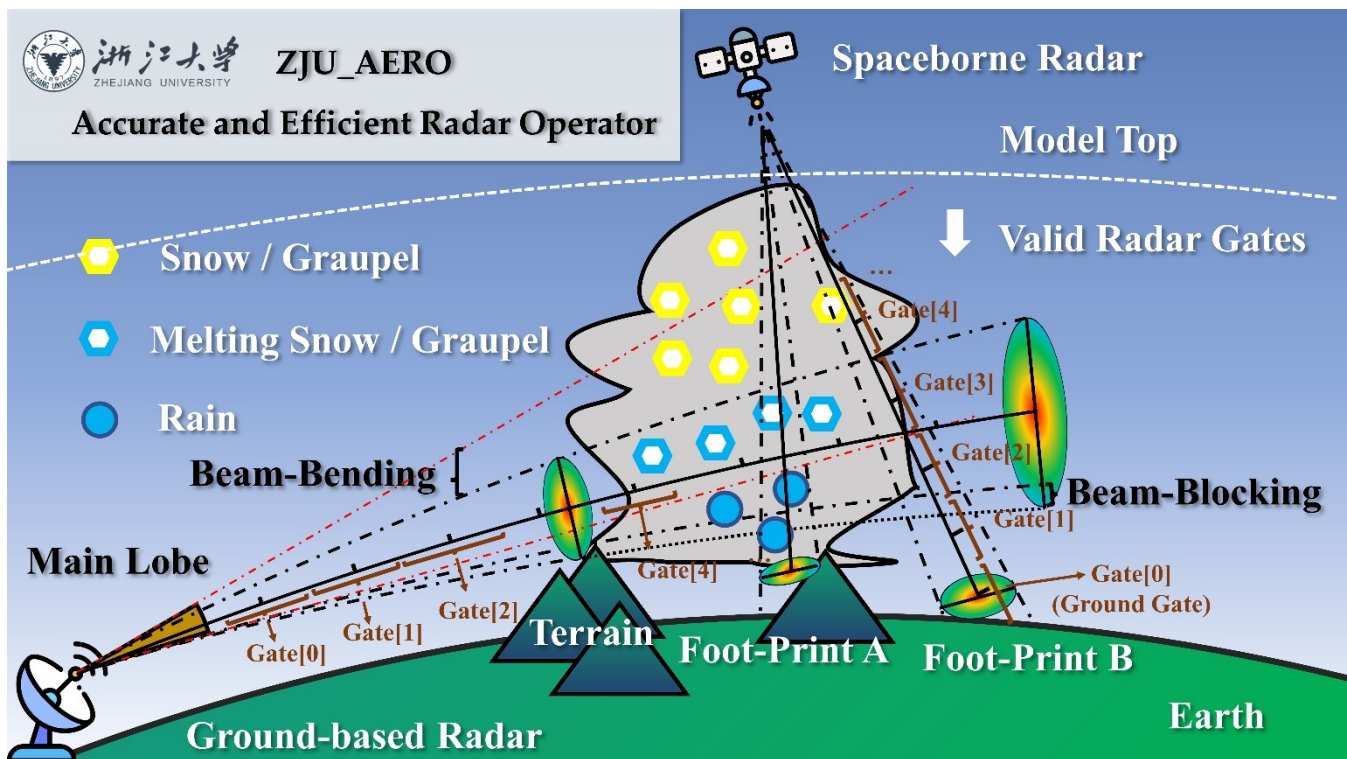
Figure 1: A conceptual graph illustrating the types of simulations that the Accurate and Efficient Radar Operator designed by
105 ZheJiang University (ZJU-AERO) can accommodate. This graph visualizes the beam-bending and beam-blocking effects, which are taken into considerations by many radar operators designed for ground-based radars. For these radars, the sampling volume within the main lobe of the radar antenna patterns increases with the range of detection, as indicated by the area between the two dashed–dotted black curves. The radar beam follows an approximately $4/3R_E$-radius curve under standard atmospheric profile conditions and is commonly referred to as beam-bending (in which R_E is the radius of the Earth). Note that the sampling volume can be partially
110 blocked by terrain as indicated by the area above the dotted black line. The space-borne radar scans, which have relatively small zenith angles (usually within 20°), are rarely affected by the beam-bending phenomenon. The radar gates of ground-based radar are recorded from the zero range-bin, while the gates of spaceborne radar are only stored within the data sampling range with respect to mean sea level, for example, GPM/DPR products only stores range-bins of altitude between –5 km and 19 km as spaceborne radars scan always cast a footprint on the earth. In ZJU-AERO, only the radar gates beneath the NWP model top,
115 known as "valid radar gates", are represented and simulated in order to save on memory usage and computational resources.

2.1 Flow Chart and Concepts

Figure 2 provides an overview of the ZJU-AERO simulation procedure for a single radar scan. ZJU-AERO consists of five modules, represented by green boxes in Fig. 2. These modules are (A): NWP interface submodule, (B) Beam submodule (decomposed into B1 and B2 for ground-based and spaceborne Radars, respectively, (C) Interpolation submodules, (D) Hydrometeor sumbmodule, and (E) Core submodule. The workflow of ZJU-AERO can be summarized as follows:

1. The NWP interface submodule (A) reads NWP prognostic variables from external storage files and interpolates the data defined on the original model grid (such as horizontal Arakawa-C grid and vertical Charney-Phillips grid in CMA–GFS/MESO (Chen et al., 2008; Shen et al., 2023)) to a regular grid on which all variables are collocated and evenly spaced horizontally (in the space of projection). The prognostic variables include hydrometeor variables (Qc, Qi, Qr, Qs, and Qg representing mixing ratios of cloud water, cloud ice, rain, snow, and graupel, respectively) and dynamic variables (U, V, W, T, P, and Q representing zonal, meridional, vertical wind, temperature, pressure, and water vapor mixing ratio, resepectively). Addtionally, static model information such as orography data defined on model grids is required for simulating partial beam blocking. This step facilitates a quick and convenient second-round interpolation from the regular model grid to the radar beam trajectories. It is worth to point it out that ZJU-AERO can also interface with the output of WRF NWP model (Skamarock et al., 2019).

2. The beam trajectory submodule (B1 and B2) calculates the propagation trajectories of the radar beam. For ground-based radar systems, the temperature and humidity profiles above the radar site are used to solve the trajectory online. Specifically, the atmosphere refractive index Na are determined from atmosphere temperature T, pressure P and water vapor mixing ratio Q. Users can choose between an online ray-tracing ordinary differential equation (ODE) solver (Zeng et al., 2014) or an offline $4/3R_E$ solver in ZJU-AERO. Multiple sub-trajectories (determined by horizontal quadrature number N $\times$ vertical quadrature number M) are sampled within the 3dB-beamwidth of the main lobe for the N$\times$M sub-trajectories. The observable radar variables are averaged with weights inferred from antenna patterns over all the sub-beams to obtain the final results (beam-broadening and beam-blocking are considered in this way). See Zeng et al. (2016) for more about sub-beam sampling and averaging methods. Nevertheless, the beam trajectory of space-borne radar is computed using the geometry shown in Figure 3, and no sub-trajectory averaging is supported at this time.

3. The interpolation submodule (C) uses a trilinear interpolation algorithm to interpolate the NWP prognostic variables to the gates of radar beam trajectories. The quick trilinear interpolations are performed in a two-step manner: (1) vertically interpolating the data defined on the eight vertices of the cube containing the radar gates to the four vertices of the horizontal box surrounding the radar gate and (2) performing bilinear interpolation; for more details see the Appendix A of Wolfensberger and Berne (2018).

4. The hydrometeor submodule (D) specifies the settings of hydrometeor in each radar gate along each trajectory. This includes the orientation preference, possibility distribution of particle morphology, particle size distribution (PSD),

and other parameters. If the particle has a regular morphology, such as a spheroid, an analytical expression can then
150   be used to retrieve the PSD. However, if an irregular morphology distribution varying with diameter is used, a numerical solver using the Newton iteration method for PSD is then applied to more precisely preserve the water concentration of hydrometeors.

5. The bulk scattering properties of particles in each radar gate are computed by integrating the single scattering properties across the size spectrum of each hydrometeor type and summing over hydrometeor types. The database
155   of particle optical properties composed three levels (Level A, Level B, and Level C), which well be introduce in detaill in Section 3.3. The Level B applied single scattering property database (see Section 3.3) is consulted in this step, while the PSD parameters have been solved in step 4.

6. The core submodule of ZJU-AERO calculates the intrinsic polarimetric radar variables on each radar gate, based on the bulk scattering properties presented in step 5. These radar variables include single-polarization reflectivities (Z_H
160   for horizontal reflectivities), dual-polarization variables (Z_{DR}, K_{DP}, δ_{hv}, Φ_{DP} and ρ_{hv} for differential reflectivity, differential phase shift, backscatter differential phase and co-polar correlation coefficient, respectively), and attenuation variables (a_H and a_V for horizontal and vertical attenuation coefficient, respectively). The defintions of there variables can be found in Section 2.2. For a detailed explanation of the intrinsic radar variables, please refer to Zhang (2016).

165 7. In the final step, the observable radar variables are obtained by taking into account the attenuation and phase shift accumulated along the beam trajectories. If quadrature numbers N and M are not set to 1 for ground-based radar simulations, antenna pattern weighted averaging would be performed.
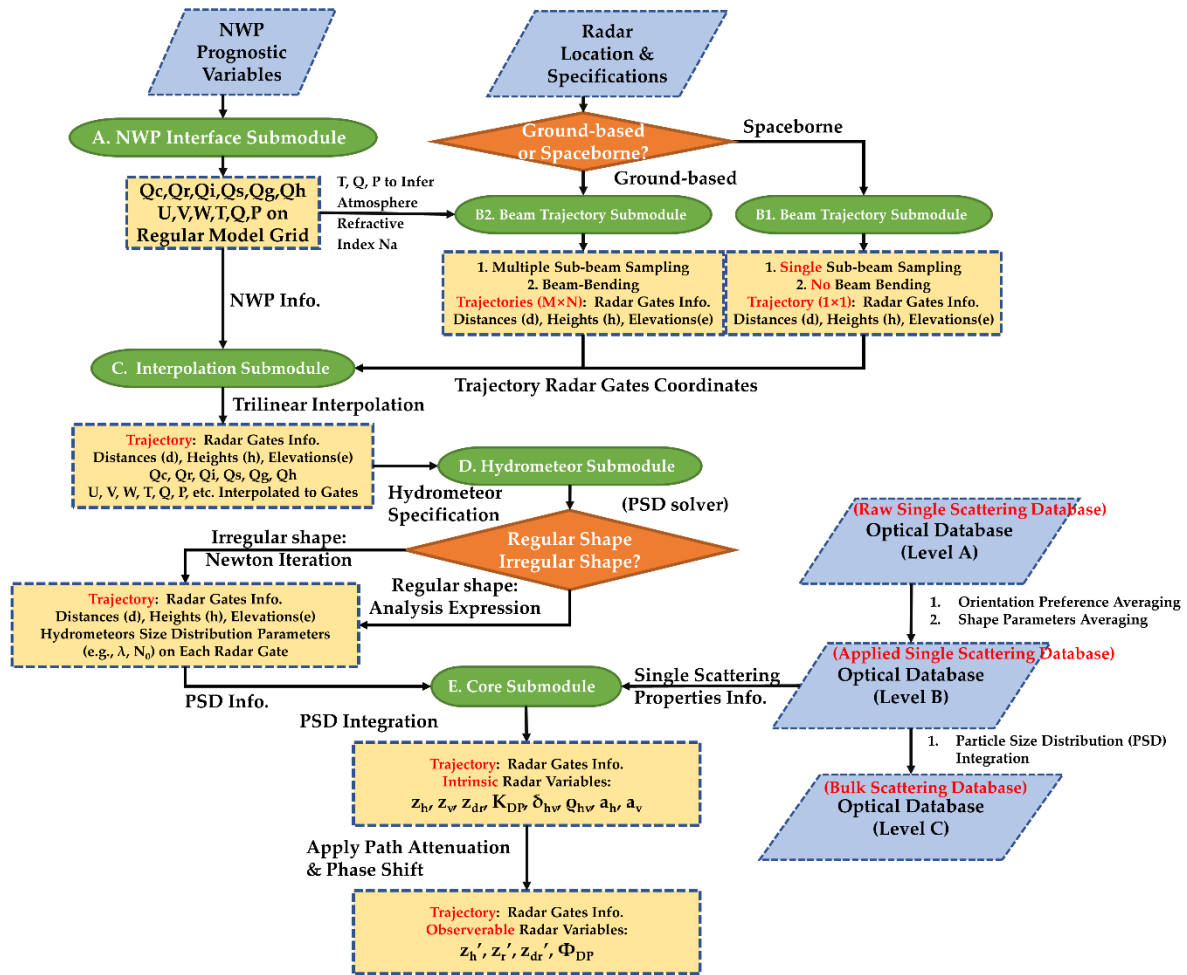
Figure 2: A conceptual flow chart of ZJU-AERO. The parallelogram boxes represent input data (including numerical weather prediction (NWP) output, radar specifications, and optical properties look-up tables). The green round rectangles indicate the names of the key submodules of ZJU-AERO. The yellow dashed boxes indicate the key data structure used in the simulations. The diamonds represent the points at which crucial "if-else" judgements can be conducted during processing.

As previously explained, the trajectory of a space-borne radar beam can be treated without considering the beam-bending effects while still maintaining precision. The WGS84 coordinates of satellites, denoted as **A (scLat, scLon, scAlt),** in addition to the centre of foot-print, **A₁ (Lat, Lon),** can be obtained through the satellite radar L1/L2 products thereafter referred to as swath files. These coordinates can then be used to calculate the local elevation angle of a given radar gate, **C,** using the knowledge of trigonometry in Figure 3(b). The length of segments **H** and **R_E** can be computed by converting the (latitude, longitude, altitude) WGS84 coordinates to the Earth-Centre–Earth-Fixed (ECEF) coordinates. The range of radar gate **AC** is provided by the space-borne radar observation system in the L1 product of GPM/DPR known as "scRangeEllipsoid" (Iguchi et al., 2010).

(a).

(b).
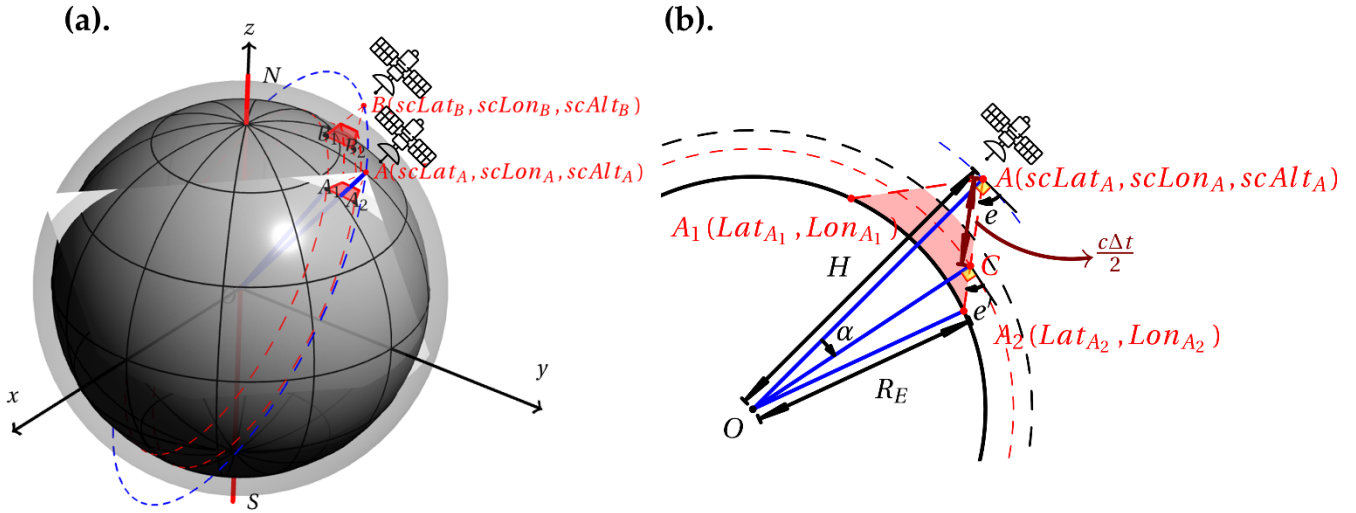
Figure 3: Conceptual graphs depicting the observation geometry of space-borne radar, with panel (a) showing a 3D graph illustrating the inclined orbit of a precipitation measuring satellite, such as the Tropical Rainfall Measuring Mission/Global Precipitation Measurement/Fengyun3-Rain Measurement (TRMM/GPM/FY3RM) with a blue dashed line. The satellite positions A and B were selected from the orbit and the triples (scLat, scLon, scAlt) on A and B were measured using the WGS84 coordinate system. The space-borne radar is capable of performing cross-track scans, creating a swath between two parallel red cycles on the Earth. The space spanned by two red isosceles trapezoids indicates that the valid scan volume in troposphere between orbit positions A and B in the troposphere. In panel (a), we selected the white plane protruding from the Earth (a plane determined by the Earth's center O in addition to the two end footprints (A₁ and A₂) of a single cross-track scan) to examine the geometric relationships in panel (b). When neglecting the beam-bending phenomenon in the space-borne radar detection, the local elevation angle, e', can be expressed as e' = e-α in which e is the elevation angle on the satellite. The angle α could be determined using trigonometry, given that AC represents the range of the radar gate C.

In this paper, we did not elaborate on the algorithm details of certain issues, such as (a) trilinear interpolation, (b) sub-beam sampling and antenna pattern weighted averaging, and (c) ray-tracing trajectory solver. Since those topics have already undergone sufficient discussions in other works concerning radar operators, and we just inherited those settings and options from them. Readers with an interest in these options may refer to the bibliography mentioned in the ZJU-AERO general workflow description text. At this point, we should specify the formulation convention used in the radar operator and move on to the non-spherical optical database design of ZJU-AERO.

2.2 Physical Basis

The amplitude scattering matrix $\mathbf{S_{FSA}}$ of a single particle is defined in Eq. (1), in which $\mathbf{E}$ indicates the vector electric field, and the superscripts "sca" / "inc" represent scattering and incident waves, respectively. The subscripts "h" and "v" indicate two decomposed components of the vector electric field in the horizontal and vertical directions, respectively. Specifically, the horizontal and vertical unit vectors are defined as unit vectors $\hat{\phi}$ and $\hat{\theta}$ of the spherical coordinate system under the Forward

Scattering Alignment (FSA) convention (see Figure 4). k_0 is the wave number in free space, and r is the distance from the

205 particle center.

$$
\begin{bmatrix} E_h^{sca} \\ E_v^{sca} \end{bmatrix} = \frac{e^{-ik_0 r}}{r} \mathbf{S_{FSA}} \begin{bmatrix} E_h^{inc} \\ E_v^{inc} \end{bmatrix} = \frac{e^{-ik_0 r}}{r} \begin{bmatrix} S_{hh} & S_{hv} \\ S_{vh} & S_{vv} \end{bmatrix}_{FSA} \begin{bmatrix} E_h^{inc} \\ E_v^{inc} \end{bmatrix}, \tag{1}
$$

Obviously, the scattering matrix relates the incident electric field to the scattered electric field, and it must have the dimension of L. In fact, the amplitude scattering matrix stored in the single-scattering database, Level A/B, is expressed in mm.

210 Although the optical properties of hydrometeors are consistently computed and stored in the FSA convention, this convention is not used for mono-static radar applications. Figure 4 explains why the Back Scattering Alignment (BSA) convention should be introduced for calculating radar variables (Chandrasekar, 2001). The incident light propagates along $-\mathbf{X_L}$ direction and comes into contact with the particle at the origin **O**. If we use the definition of h and v unit vectors under the FSA convention, the horizontal unit vector of backscattering light is then inconsistent with the incident light,

215 $(\hat{h}_{FSA}^{inc}, \hat{v}_{FSA}^{inc}, \hat{k}_{FSA}^{inc}) = (-\hat{h}_{FSA}^{bsca}, \hat{v}_{FSA}^{bsca}, -\hat{k}_{FSA}^{bsca})$, in which "bsca" indicates backscattering light. To resolve this convention conflict between polarimetric radar observation system and scattering computation, BSA forces the following relationship by reversing the direction of the backscattering horizontal unit vector definition: $(-\hat{h}_{FSA}^{bsca}, \hat{v}_{FSA}^{bsca}, -\hat{k}_{FSA}^{bsca}) = (\hat{h}_{BSA}^{bsca}, \hat{v}_{BSA}^{bsca}, \hat{k}_{BSA}^{bsca})$.

$$
\begin{bmatrix} S_{hh} & S_{hv} \\ S_{vh} & S_{vv} \end{bmatrix}_{BSA} = \begin{bmatrix} -1 & 0 \\ 0 & 1 \end{bmatrix} \begin{bmatrix} S_{hh} & S_{hv} \\ S_{vh} & S_{vv} \end{bmatrix}_{FSA} = \begin{bmatrix} -S_{hh} & -S_{hv} \\ S_{vh} & S_{vv} \end{bmatrix}_{FSA}, \tag{2}
$$

Hence, the amplitude scattering matrix in the BSA convention is related to that of FSA in Eq. (2). The following amplitude

220 scattering elements used for polarimetric radar variables computation are represented in the BSA convention unless otherwise stated (namely, a conversion is needed in the core submodule before obtaining radar variables).
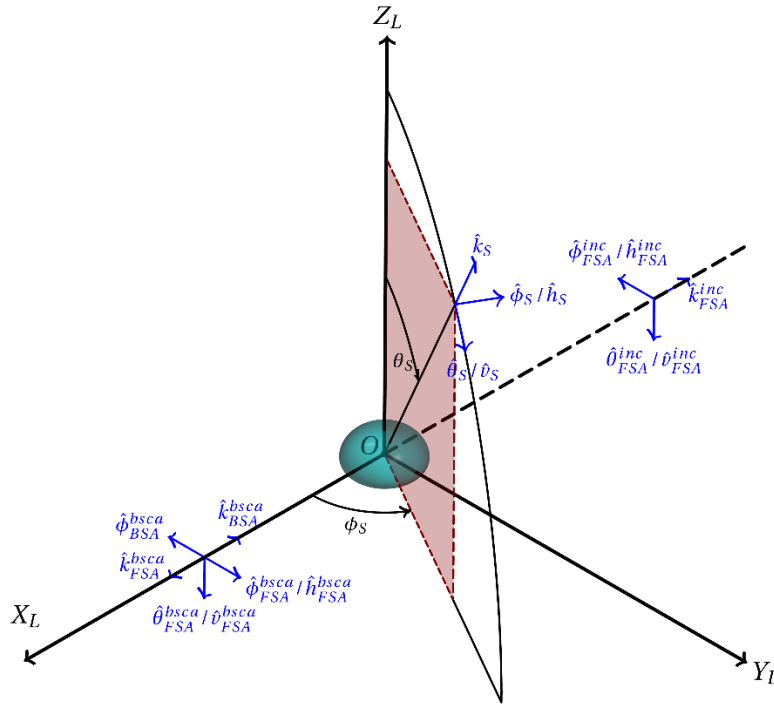
Figure 4: The unit vectors in the definition of the amplitude scattering matrix. We assumed that the particle was located at the origin of the laboratory coordinate system, and the incident light propagated along the $-X_L$ direction. The unit vectors subscripted with Forward Scattering Alignment (FSA) are unit vectors defined in the FSA convention, while unit vectors defined by Back Scattering Alignment (BSA) convention are indicated by subscription BSA.

Apart from the 2×2 complex amplitude scattering matrix $\mathbf{S}$, we also have the 4×4 real matrix, known as Mueller matrix, $\mathbf{Z}$, and extinction matrix, $\mathbf{K}$, which describe polarimetric light scattering properties of particles in the Stokes vector space. We kept the definition of $\mathbf{Z}$ and $\mathbf{K}$ consistent with those mentioned in a study by Mishchenko (2014). The Mueller and extinction matrices can be derived from the amplitude scattering matrix. Specifically, the forward scattering amplitude matrix show a linear relationship with $\mathbf{K}$, while the backscattering amplitude matrix can be used to calculate $\mathbf{Z}$ in backscattering geometry. The elements of $\mathbf{Z}$ and $\mathbf{K}$ are both in the dimension of L^2 (namely, they were stored in the units of mm^2).

$$\langle\mathbf{X}\rangle = \int_0^\infty \mathbf{X}(D)\,N(D)\mathrm{d}D, \quad \mathbf{X} = \mathbf{Z}, \mathbf{K}, \tag{3}$$

As shown in Eq. (3), we could compute the bulk-scattering properties $\langle\mathbf{X}\rangle$ used in the expression of several polarimetric radar variables by performing size distribution integrations over elements of $\mathbf{Z}$ and $\mathbf{K}$ matrices. Here, $N(D)$ represents the

number concentration distribution function in units of mm^{-1}·m^{-3} over the particle spectrum, and D is the diameter[1] of the hydrometeor in units of mm. The elements of bulk matrices $\langle \mathbf{Z} \rangle$ and $\langle \mathbf{K} \rangle$ were expressed in units of mm^2·m^{-3}.

Note that we can only apply the integration over the complex amplitude scattering matrix, $\mathbf{S}$, unless in the forward scattering geometry, which is fundamentally associated with the optical theorem (Yang et al., 2011). This is because integrating over extinction matrix elements is proportional to integrating corresponding forward amplitude scattering matrix elements. For example:

$$\langle K_{11} \rangle = \frac{2\pi}{k_0} \langle S_{hh} \rangle + \frac{2\pi}{k_0} \langle S_{vv} \rangle,$$ (4)

Next we describe how to calculate intrinsic radar variables calculation using bulk matrices $\langle \mathbf{Z} \rangle$ and $\langle \mathbf{K} \rangle$:

1. Horizontal/Vertical reflectivity $z_{h/v}$ in units of mm^6·m^{-3}:

$$z_{h/v} = \frac{\lambda^4}{\pi^5 |K_w|^2} \int_0^\infty \sigma_{bsca,h/v} \, \mathrm{N}(D)\mathrm{d}D = \frac{4\pi\lambda^4}{\pi^5 |K_w|^2} \int_0^\infty |S_{vv/hh}|^2 \, \mathrm{N}(D)\mathrm{d}D$$

$$= \frac{2\lambda^4}{\pi^4 |K_w|^2} \int_0^\infty (Z_{11} \pm Z_{12} \pm Z_{12} + Z_{22}) \, \mathrm{N}(D)\mathrm{d}D \quad ,$$ (5)

$$= \frac{2\lambda^4}{\pi^4 |K_w|^2} \left(\langle Z_{11} \rangle \pm \langle Z_{12} \rangle \pm \langle Z_{21} \rangle + \langle Z_{22} \rangle \right)$$

in which $\sigma_{bsca,h/v}$ indicates the horizontal/vertical backscattering cross-section of a particle (namely, $\sigma_{bsca,h/v} = 4\pi |S_{hh/vv}|^2$), and '$\pm$'s become negative for z_h but positive for z_v. λ is the wavelength of radar, $K_w = |(\varepsilon_w - 1)/(\varepsilon_w + 2)|$ is the dielectric factor (ε_w is the dielectric constant of water at the wavelength of radar for a fixed temperature of 283.15 K).

2. Differential reflectivity z_{dr} without dimension:

$$z_{dr} = \frac{z_h}{z_v} = \frac{\langle Z_{11} \rangle - \langle Z_{12} \rangle - \langle Z_{21} \rangle + \langle Z_{22} \rangle}{\langle Z_{11} \rangle + \langle Z_{12} \rangle + \langle Z_{21} \rangle + \langle Z_{22} \rangle},$$ (6)

3. Specific differential phase shift (deg.·km^{-1}) upon propagation, K_{DP}, is defined by

---

[1] In the weather radar community, the particle diameter D usually refers to equal-volume-sphere diameter for a liquid hydrometeor, while D is often regarded as maximum dimension when describing solid and melting types of hydrometeors.

$$K_{DP} = 10^{-3} \cdot \frac{180}{\pi} \cdot \lambda \int_0^\infty \Re(S_{hh}^{fwd} - S_{vv}^{fwd}) \, \mathrm{N}(D)\mathrm{d}D = 10^{-3} \cdot \frac{180}{\pi} \cdot \int_0^\infty \frac{2\pi}{k_0} \Re(S_{hh}^{fwd} - S_{vv}^{fwd}) \, \mathrm{N}(D)\mathrm{d}D$$

$$= 10^{-3} \cdot \frac{180}{\pi} \cdot \langle K_{34} \rangle \tag{7}$$

Here, 10^{-3} in Eq. (7) represents the coefficient in unit conversion from mm²·m⁻³ to km⁻¹, and the coefficient $180/\pi$ is used to convert the unit of result from radii·km⁻¹ to deg.·km⁻¹.

255   4.   The one-way linear-scale attenuation coefficient[2] of horizontal/vertical polarization $a_{h/v}$ in units of km⁻¹ :

$$a_{h/v} = 10^{-3} \int_0^\infty \sigma_{ext,h/v} \, \mathrm{N}(D)\mathrm{d}D = 10^{-3} \int_0^\infty \frac{4\pi}{k_0} \Im(S_{hh/vv}^{fwd}) \, \mathrm{N}(D)\mathrm{d}D$$

$$= 10^{-3} \int_0^\infty (K_{11} \pm K_{12}) \, \mathrm{N}(D)\mathrm{d}D = 10^{-3} \left(\langle K_{11} \rangle \pm \langle K_{12} \rangle \right) \tag{8}$$

in which "±"s turn negative for a_h but positive for a_v. Again, 10^{-3} in Eq. (8) serves as the coefficient in unit conversion from mm²·m⁻³ to km⁻¹. $\sigma_{ext,h/v}$ indicates horizontal/vertical extinction cross-section of a given particle (i.e.,

$$\sigma_{ext,h/v} = \frac{4\pi}{k_0} \Im\left(S_{hh/vv}^{fwd} \right)).$$

260   5.   Total differential phase shift upon backscattering δ_{hv} in units of deg. is represented as shown below:

$$\delta_{hv} = \frac{180}{\pi} \angle \left(\int_0^\infty S_{hh} S_{vv}^* \, \mathrm{N}(D)\mathrm{d}D \right) = \frac{180}{\pi} \angle \left(\int_0^\infty \left[0.5(Z_{33} + Z_{44}) + 0.5(Z_{43} - Z_{34})i \right] \mathrm{N}(D)\mathrm{d}D \right)$$

$$= \frac{180}{\pi} \angle \left(\left[\langle Z_{33} \rangle + \langle Z_{44} \rangle \right] + \left[\langle Z_{43} \rangle - \langle Z_{34} \rangle \right] i \right) \tag{9}$$

The notation '$\angle$' in Eq. (9) indicates the amplitude of the complex value. The coefficient $180/\pi$ is used to convert the unit of result from radii to deg. Again.

6.   Co-polar correlation coefficient ρ_{hv} without dimension:

---

[2] The one-way specific attenuation in dB-scale $\alpha_{h/v}$ in units of dB·km⁻¹, which relates to the linear-scale attenuation coefficient by

$\alpha_{h/v} = 10\log_{10}(e) \cdot a_{h/v} = 4.343 \cdot a_{h/v}$, is also used in many studies of weather radar that consider the change of logarithm-base from e to 10.

$$\rho_{hv} = \frac{\left|\int_0^\infty S_{hh}S_{vv}^* \,\mathrm{N}(D)\mathrm{d}D\right|}{\sqrt{\int_0^\infty |S_{hh}|^2 \,\mathrm{N}(D)\mathrm{d}D \cdot \int_0^\infty |S_{vv}|^2 \,\mathrm{N}(D)\mathrm{d}D}} = \frac{\left|\int_0^\infty \left[0.5(Z_{33}+Z_{44})+0.5(Z_{43}-Z_{34})i\right]\mathrm{N}(D)\mathrm{d}D\right|}{\sqrt{\int_0^\infty 0.5(Z_{11}-Z_{12}-Z_{21}+Z_{22})\,\mathrm{N}(D)\mathrm{d}D \cdot \int_0^\infty 0.5(Z_{11}+Z_{12}+Z_{21}+Z_{22})\,\mathrm{N}(D)\mathrm{d}D}} , (10)$$

$$= \frac{\left|(\langle Z_{33}\rangle + \langle Z_{44}\rangle) + (\langle Z_{43}\rangle - \langle Z_{34}\rangle)i\right|}{\sqrt{(\langle Z_{11}\rangle - \langle Z_{12}\rangle - \langle Z_{21}\rangle + \langle Z_{22}\rangle)\cdot(\langle Z_{11}\rangle + \langle Z_{12}\rangle + \langle Z_{21}\rangle + \langle Z_{22}\rangle)}}$$

In Eq. (10), the co-polar correlation coefficient ρ_{hv} is the magnitude of complex co-polar correlation coefficient $\widetilde{\rho_{hv}}$, whose amplitude is the total differential phase shift upon backscattering in Eq. (9).

Please note that the summation over hydrometeor types were omitted in Eqs.(5)-(10) for the sake of clarity. Readers can easily obtain the more complicated real expressions of radar variables by applying extra summations over hydrometeor types for $\langle \mathbf{Z} \rangle$ and $\langle \mathbf{K} \rangle$ elements before carrying out calculations.

The aforementioned radar variables $z_{h/v}$, $a_{h/v}(\alpha_{h/v})$, z_{dr}, K_{DP}, δ_{hv} and ρ_{hv} are often referred as intrinsic radar variables determined by the atmosphere and hydrometeor conditions in local radar gates. Nevertheless, under the assumption of first-order multiple scattering model, although the wave is scattered only once before it is received, the two-way propagation effects such as attenuation and phase-shift are taken into account by using the wave number of effective medium composed of air and hydrometeors along the beam trajectory (Zhang, 2016). We can derive the observable radar variables as shown below:

$$z'_{h/v}(r_g) = z_{h/v}(r_g)\cdot \exp\left(-2\int_{r=0}^{r=r_g} a_{h/v}(r)\mathrm{d}r\right), \tag{11}$$

$$\Phi_{DP}(r_g) = 2\int_{r=0}^{r=r_g} K_{DP}(r)\mathrm{d}r + \delta_{hv}(r_g), \tag{12}$$

In Eq. (11)-(12), r_g is the range of the radar gate, the variable of integration r is the range along the radar beam trajectory. $z'_{h/v}$ marked with a prime is the horizontal / vertical observable reflectivity factor of the radar gate, attenuated on the way from transmitter to the particle and the way back from particle to the receiver. Φ_{DP} is the total phase shift interpreted as the differential phase shift upon two-way propagation plus the differential phase shift upon backscattering.

$$Z'_{H/V} = 10\log_{10}\left(z'_{h/v}\right), \tag{13}$$

$$Z'_{DR} = 10\log_{10}\left(z'_{dr}\right) = 10\log_{10}\left(\frac{z'_h}{z'_v}\right), \tag{14}$$

Geoscientific
Model Development
Discussions

Eqs. (13) and (14) give the observable horizontal / vertical reflectivity $Z'_{H/V}$ in units of dBZ and differential reflectivity Z'_{DR}

285 in units of dB.

2.3 Hydrometeors specifications

Table 1: An overview of the specification for all categories of hydrometeors in the Accurate and Efficient Radar Operator designed by Zhejiang University (ZJU-AERO). Some sophisticated specifications are only tagged with a bibliography and explained with more details in the context to make this table more compact and convenient for reference.

Hydrometeor Category	Shape Parameters	Mass-Diameter Relationship	Refractive Index Model	Orientation Preference	Particle Size Distribution
Rain[1]	Option A1: Spheroid (Brandes et al., 2002)	PSD model Using Equal-Volume-Sphere Diameter: $m(D_{eq}) = aD_{eq}^b$ $(a = \frac{\pi}{6}\rho_w, b = 3)$	Option B1: (Ellison, 2007)	$p(\beta) \propto \sin(\beta) \cdot$ $\exp\left(-\frac{\beta}{2\sigma_\beta^2}\right)$ $(\sigma_\beta = 7 \deg.)$ (Chandrasekar, 2001)	Option C1: (Marshall and Palmer, 1948) / Option C2: (Thompson et al., 2008) / Option C3: (Wang et al., 2016) / Option C4: (Abel and Boutle, 2012)
	Option A2: Chebyshev (Chuang and Beard, 1990)		Option B2: (Liebe et al., 1991) (deprecated)		
Snow	Spheroid (Garrett et al., 2015)	Option A1: $\bar{m}(D_{max}) = aD_{max}^b$ $(a = \frac{\pi}{6}\rho_{snow}, b = 3)$	Air–ice matrix using Maxwell–Garnett effective medium approximation	$p(\beta) \propto \sin(\beta) \cdot$ $\exp\left(-\frac{\beta}{2\sigma_\beta^2}\right)$ $(\sigma_\beta(D_{max}) = 40.0D_{max}^{-0.077} \deg.)$ (Garrett et al., 2015)	Temperature-dependent PSD model: (Field et al., 2005)
		Option A2: $\bar{m}(D_{max}) = \rho_{ice} \cdot V_{ice}(D_{max})$			
Graupel	Spheroid (Garrett et al., 2015)	Option A1: $\bar{m}(D_{max}) = aD_{max}^b$ $(a = \frac{\pi}{6}\rho_{graupel}, b = 3)$	Air–ice matrix using Maxwell–Garnett effective medium approximation	$p(\beta) \propto \sin(\beta) \cdot$ $\exp\left(-\frac{\beta}{2\sigma_\beta^2}\right)$ $(\sigma_\beta(D_{max}) = 58.07D_{max}^{-0.11} \deg.)$ (Garrett et al., 2015)	Option B1: Microphysics scheme WSM6 (Hong and Lim, 2006) / Option B2: Microphysics scheme Thompson (Thompson et al., 2008)
		Option A2: $\bar{m}(D_{max}) = \rho_{ice} \cdot V_{ice}(D_{max})$			

290 [1] The specifications regarding the hydrometeor category of rain are discussed in Section 3.

Table 1 summarizes the hydromteor specifications in ZJU-AERO, with the following important notes:

(1). During the early development stage of ZJU-AERO, we initially used the dielectric model for water proposed by Liebe et al. (1991). However, we transitioned to a more accurate and contemporary dielectric model developed by Ellison (2007).

295 Nevertheless, we retained the outdated option and optical property look-up table from the old dielectric model in our archive for future reference and comparison (see the column of refractive index model in Table 1).

(2). In principle, it is encouraged to use PSD schemes compatible with the microphysics package in the NWP model to ensure consistent hydrometeors settings in simulations. Therefore, ZJU-AERO, which was designed for CMA–GFS/MESO, provides

PSD options that are compatible with the single-moment microphysics scheme WSM6 (Hong and Lim, 2006) and Thompson

300   (Thompson et al., 2008), which are widely used in global and regional operational models of CMA. For instance, option C1

for rain and option B1 for graupel are compatible with the WSM6 package, while option C2 for rain and option B2 for graupel

are compatible with the Thompson package (see the column of particle size distribution in Table 1). However, for the snow

category, we implemented the PSD scheme of Field et al. (2005) as the only option since it is the widely acknowledged as the

best globally applicable temperature-dependent PSD model for solid precipitation. Additionally, we have provided users with

305   some additional PSD schemes for sensitivity assessment, such as option C3 (Wang et al., 2016) and C4 (Abel and Boutle,

2012) for the rain category. Those PSD schemes in the ZJU-AERO that are incompatible with the microphysics package used

in the NWP model are referred to as "forced" PSD schemes.

(3). Solid hydrometeor categories, such as snow and graupel, are known to have relatively larger uncertainties associated with

parameterizations of aspect ratios and orientation preference. To address these uncertainties, a field research study was

310   conducted using an *in-situ* observation instrument called the multi-angle snowflake camera (MASC), as described by Garrett

et al. (2012). This instrument was used to measure the aspect ratios and orientations of over 30,000 solid particles in the Eastern

Swiss Alps. The particles were then classified into aggregates (corresponding to the snow category in this study), rimed, and

graupel, as described in Garrett et al. (2015). The fitted model from this study was used as a *priori* knowledge of hydrometeor

shape specifications in the ZJU-AERO (see the column of shape parameters in Table 1).

315    $$p(\gamma; D_{max}) \propto (\gamma - 1)^{\Lambda(D_{max}) - 1} \exp\left(\frac{\gamma - 1}{M(D_{max})}\right),$$ (15)

Eq. (15) provides the possibility distribution function of the aspect ratio, in which γ is the reciprocal of the aspect ratio. It is

assumed to follow a gamma distribution with an offset coefficient of 1 (i.e., $\gamma > 1$). The shape coefficient, $\Lambda(D_{max})$, and

a scale coefficient, $M(D_{max})$, are functions of particle maximum dimension. We used the power-law relationships of

$\Lambda(D_{max})$ and $M(D_{max})$ that were fitted by Wolfensberger and Berne (2018):

320    $$\Lambda_{snow}(D_{max}) = 8.42 D_{max}^{-0.57}; M_{snow}(D_{max}) = 0.053 D_{max}^{-0.79}$$
$$\Lambda_{graupel}(D_{max}) = 3.2 D_{max}^{-0.42}; M_{graupel}(D_{max}) = 0.074 D_{max}^{-0.67},$$ (16)

(4). The mass–diameter relationship is crucial in determining the PSD (see the column of mass-diameter relationship in

Table 1). For instance, the hydrometeor category follows the gamma distribution (the widely used exponential distribution is

just a special case of gamma distribution when $\mu = 1$):

$$N(D) = N_0 D^{\mu} e^{-\lambda D}$$ (17)

325   in which N_0 is the intercept, λ is the slope and μ is the shape coefficient of that gamma distribution. As is often the case,

μ is a prescribed constant in the microphysics package, while N_0 either equals a prescribed constant or relates to λ by a

power-law, in which x_1 and x_2 are parameters fitted by drop size distribution (DSD) observations (see Section 3.4):

$$N_0 = x_1 \lambda^{x_2} \tag{18}$$

If a hydrometeor category is of single-moment microphysics scheme, then given the mass concentration Q_x in units of

330   kg·m^{-3}, we can solve the unknown parameter λ and determine all relevant PSD information that pertains to that radar gate:

$$Q_x = \int_0^\infty \overline{\mathrm{m}}(D) \cdot \mathrm{N}(D)\mathrm{d}D , \tag{19}$$

If the mass–diameter relationship can be approximated as power-law form $\overline{\mathrm{m}}(D) = aD^b$, in which $\overline{\mathrm{m}}(D)$ is the average

mass of a given size of a particle (considering that some hydrometeor categories have a possibility distribution over shape

parameters such as aspect ratio). Then λ can be solved analytically by plugging Eq. (17) into Eq. (19):

335    $$\lambda = \left[\frac{ax_1\Gamma(1+b+\mu)}{Q_x} \right]^{\frac{1}{1+b+\mu-x_2}} , \tag{20}$$

Again, it seems that a microphysics-consistent mass–diameter relationship $\overline{\mathrm{m}}\left(D_{max}\right) = \frac{\pi}{6}\rho_{sp}D_{max}^{\;3}$ for snow and graupel

would be preferable. Many microphysics schemes, such as WSM6, simply treated solid precipitation categories as spheres

with different ice–air mixture ratios and hence different densities ρ_{sp}. However, this practice can result in a huge

inconsistency between the mass concentration represented by radar operators and the microphysics schemes since the actual

340   average mass of a given size bin is represented by the following possibility-weighted averaging over the aspect ratio for solid

hydrometeors as shown below:

$$\overline{\mathrm{m}}(D_{max}) = \int_1^\infty \mathrm{p}(\gamma; D_{max}) \mathrm{m}(\gamma; D_{max})\mathrm{d}\gamma , \tag{21}$$

It turns out that fitting Eq. (21) into power-laws was troublesome when the possibility distribution function $\mathrm{p}(\gamma; D_{max})$

varied dramatically with diameter. This problem will become even worse when we introduce other non-spherical particles,

345   such as snowflakes.

To resolve this error when using a traditional mass-diameter relationship, we implemented a benchmark PSD solver

employing a numerical method (namely, Newton–iteration) for particles with complicated morphology specifications. The

simplest case, a PSD represented by an exponential distribution with a fixed intercept parameter N_0, can be used as an

example:

$$Q_x = \sum_{D_i=D_{min}}^{D_i=D_{max}} \overline{m}(D_i) N(D_i) \Delta D = \sum_{D_i=D_{min}}^{D_i=D_{max}} \overline{m}(D_i) N_0 e^{-\lambda D_i} \Delta D$$

350

$$F(\lambda) = \sum_{D_i=D_{min}}^{D_i=D_{max}} \overline{m}(D_i) N_0 e^{-\lambda D_i} \Delta D - Q_x \qquad\qquad , \qquad\qquad (22)$$

$$F'(\lambda) = - \sum_{D_i=D_{min}}^{D_i=D_{max}} \overline{m}(D_i) N_0 e^{-\lambda D_i} D_i \Delta D$$

in which the integration in Eq. (19) is truncated within a specific diameter range of $\left[D_{min}, D_{max} \right]$ and further discretized as a

summation. The expression of the exponential distribution is then substituted in for the second equality. $\overline{m}(D_i)$ at

discretized size bins is precomputed by Eq. (21) and treated as a constant. The mass $m(\gamma; D_i)$ for each morphology

specifications can be calculated as the density of the pure ice ρ_{ice} multiplied by the volume occupied by the non-spherical

355   model $V(\gamma; D_i)$.

Based on the above formulation, the iteration relationship to derive the (n+1)-th guess λ_{n+1} from the n-th guess λ_n can be

expressed as shown below:

$$\lambda_{n+1} = \lambda_n - \frac{F(\lambda_n)}{F'(\lambda_n)}, \qquad\qquad (23)$$

While performing iterations online (the benchmark PSD solver) may lead to a decrease in the efficiency of the ZJU-AERO,

360   this problem can be resolved by using BSP LUTs instead of SSP LUTs (see Section 3.5).

3 Database of Hydrometeor Optical Properties

In Section 2, we provide a comprehensive description of the design of ZJU-AERO. Specifically, we now emphasize that the

hydrometeor optical properties database includes the elements of $\mathbf{Z}$ and $\mathbf{K}$ in units of mm^2 for single-scattering properties

and those of $\langle \mathbf{Z} \rangle$ and $\langle \mathbf{K} \rangle$ in units of mm$^2 \cdot$m^{-3} for bulk-scattering properties, both in the FSA convention.

365   Furthermore, ZJU-AERO now encompasses three types of hydrometeors: (1) rain, (2) snow, and (3) graupel. Among these

hydrometeors, the rain category offers a non-spherical shape parameter option, known as the Chebyshev shape. This shape

differs from the traditional spheroid shape commonly used in other radar observation operators. Therefore, in this section, we

will delve into the design of the database (LUT) in ZJU-AERO with more details, using the Chebyshev raindrop as an illustrative example.

3.1 The Multi-Layered Architecture

The ZJU-AERO optical property database is designed with a multi-layered architecture consisting of three levels: (1) the raw single-scattering properties (RSSP) database (level A), (2) the applied single-scattering properties (ASSP) database (level B), and (3) the bulk-scattering properties (BSP) database (level C). These levels are described in detail in Table 2.

The RSSP-Level A database contains the optical properties of individual particles without any averaging or integration over the shape parameters and orientations, which normally consumed a significant amount of memory resources ($\sim 10^1$GB). However, using the RSSP in ZJU-AERO would require online integration of orientations and shape parameters, leading to a significant slow down in radar operator performance. On the other hand, if shape and orientation averaging were applied during the the creation of the database and the raw optical data (RSSP) are discarded, the resulting database would lack the flexibility needed for modifying the shapes and orientations distributions. Additionally, future enhancements to the ZJU-AERO database may involve incorporating more sophisticated shape parameters for the non-spherical hydrometeors. Therefore, retaining the RSSP-Level A database is essential to accommodate uncertainties and increase the convenience in experiments and simulations related to shape and orientation parameters.

Building on the RSSP-Level A database, the ASSP-LevelB database improves the computational efficiency by carrying out averaging or orientation over shape parameters and orientations offline. Finally, the BSP-Level C optical database integrates the optical properties stored in the ASSP-Level B database over PSD and enables fast batch runnings in ZJU-AERO for operational use. In summary, the multi-layered architecture of the lookup table (stored in netCDF4 format) is to strike a balance between the flexibility of the database and the computational efficiency required by radar operators. Future releases of ZJU-AERO will provide software tools for flexible conversions between the database levels, allowing users to easily configure integration parameters.

Table 2: The architecture design of the multi-layered hydrometeor optical properties database used in ZJU-AERO. The column "Volume" gives an estimation of the external storage that a single database for one hydrometeor and one frequency occupies. Note that only the order of magnitude of storage space was shown in those entries.

Database Layer	Dimensions	Variables	Volume
Raw Single Scattering Properties (RSSP) Database - Level A	Shape parameters: e.g., reciprocal of aspect ratio γ Observation geometry: elevation e Orientation preference: Euler angle β Temperature: T Diameter: D_{eq} / D_{max}	Z and K in units of mm^2	$\sim 10^1$ GB

18

Applied Single Scattering Properties (ASSP) Database - Level B	Observation geometry: elevation **e** Temperature: **T** Diameter: **D$_{eq}$** / **D$_{max}$**	$\mathbf{Z}$ and $\mathbf{K}$ in units of mm^2	~10^1 MB
Bulk Scattering Properties (BSP) Database - Level C	Observation geometry: elevation **e** Temperature: **T** Mass concentration: **Q$_X$**	$\langle \mathbf{Z} \rangle$ and $\langle \mathbf{K} \rangle$ in units of mm$^2 \cdot m^{-3}$	~10^1 MB

3.2 Orientation and Observation Geometries

Figure 5 depicts the Cartesian coordinate system used to determine the orientation and observation geometries of a hexagonal plate particle. The laboratory coordinate system, denoted as OX$_L$Y$_L$Z$_L$, was aligned by vertically positioning its OZ$_L$ axis and placing its OX$_L$ axis in the vertical plane specified by the incident radar beam and OZ$_L$ This alignment sets the azimuthal angle ϕ_{inc} of the radar beam to 0. In Figure 5(a), the direction of the radar beam is shown, which is practically specified using the elevation angle $e \in [-\pi/2, \pi/2]$. For ground-based radar, this angle is positive, while for space-borne radar, it is negative. In this context, the polar angle of the radar beam, denoted as θ_{inc}, is related to the elevation angle through $\theta_{inc} = \pi/2 - e$. The shape of particle is defined in the particle coordinate system OX$_P$Y$_P$Z$_P$. In the specific example shown in Figure 5(d), the OZ$_P$ axis was set perpendicular to the basal face of a hexagonal plate. The origin O was placed at the mass center of the particle, and the OY$_P$ axis intersected two opposite vertices of the hexagonal basal face. Using the ZYZ convention of the Euler angles specified by α, β, and γ (rotations were performed with respect to the OZ, OY, and OZ axis, respectively), we could uniquely determine an arbitrary orientation of a given particle (see Figure 5(b)–(d)).

With a specified orientation and observation geometries, we can now outline the procedures for computing scattering properties of particles with arbitrary orientation preferences:

1. We used the T-matrix code to compute the T-matrix only once for a given particle and a radar beam wavelength. For both axially symmetric and homogenous particles, we used the EBCM T-matrix code (Mishchenko and Travis, 1994), while for particles without axial symmetry or those that are inhomogeneous, we applied the invariant-imbedding T-matrix (IITM) code (Bi et al., 2013; Bi and Yang, 2014; Bi et al., 2022; Wang et al., 2023).

2. With the T-matrix computed in Step 1, we efficiently calculated the forward and backward amplitude scattering matrix $\mathbf{S_{FSA}}$ in Eq. (1) for tuples of observation and orientation geometries (α, β, γ, and e) using the method of Mishchenko (2000).

3. The forward and backward amplitude scattering matrices $\mathbf{S_{FSA}}$ were then converted into the backscattering Muller and extinction matrices, $\mathbf{Z}$ and $\mathbf{K}$, respectively.

4. When averaging over α and γ, we considered that the atmosphere is generally horizontally isotropic on the scale of hydrometeor particles. It is believed that they should have no preference for Euler angles α and γ, except for extreme
420   conditions such as lightning-induced reorientation of ice crystals (Hubbert et al., 2010). Therefore, we performed internal averaging over α and γ for elements of $\mathbf{Z}$ and $\mathbf{K}$ in the scattering computation code before generating the RSSP – Level A database (see Eq. (24)). Hence, the Level A database only has two residual orientations and observation geometry dimensions: (1) $\mathbf{e}$ and (2) $\boldsymbol{\beta}$, allowing for a reasonable volume for archiving.
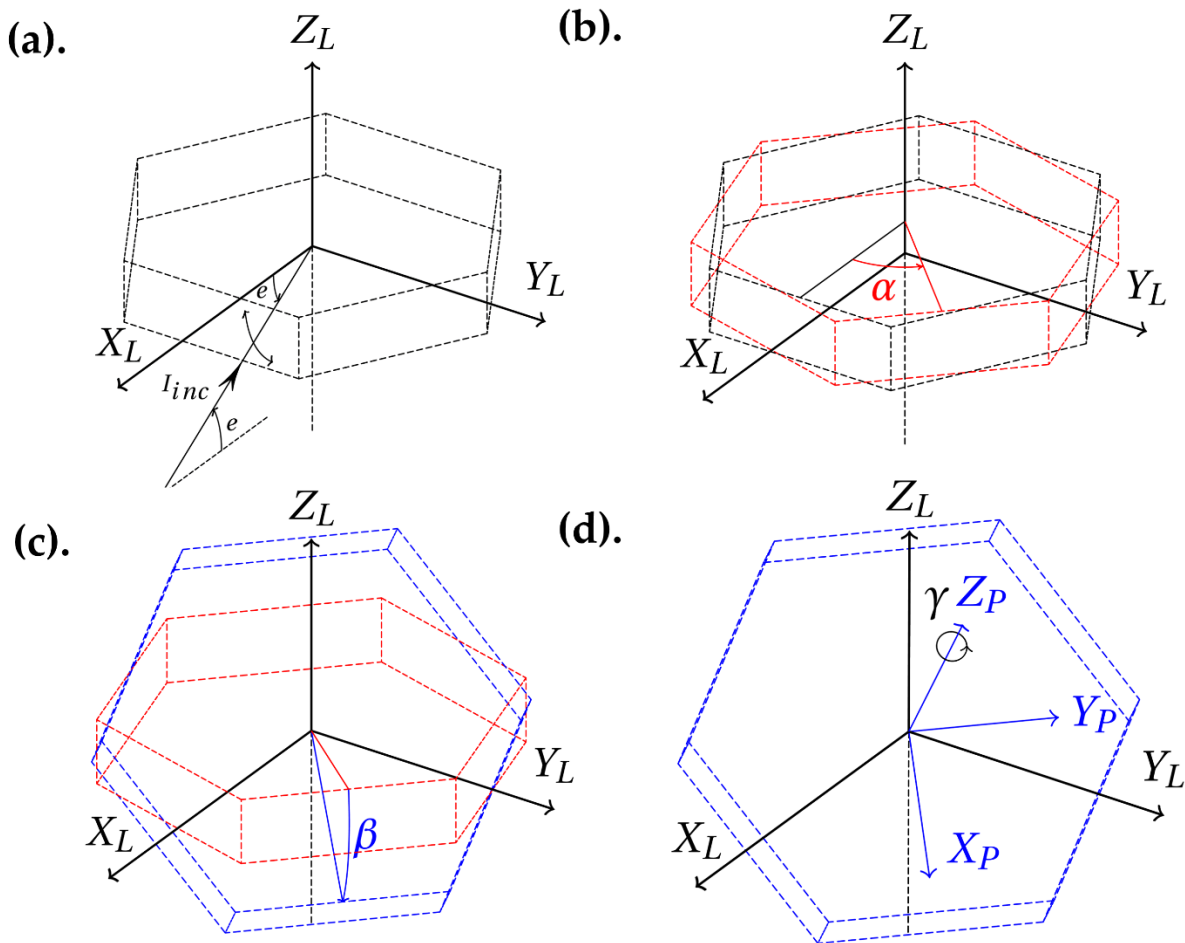
Figure 5: Illustration of the orientation preference of a particle specified with Euler angles (α, β, γ) in which a hexagonal plate was used as an example. Panel (a) shows the laboratory coordinate system $OX_LY_LZ_L$ and the particle with original orientation. The incident beam comes from the elevation angle of e. Panels (b), (c), and (d) depicts how angles α, β, and γ uniquely determine the orientation of a particle, respectively. The particle coordinate system $OX_PY_PZ_P$ is shown in panel (d) with solid blue lines.

$$430 \quad \overline{\mathbf{X}}(e,\beta) = \frac{1}{4\pi^2} \int_0^{2\pi} \mathrm{d}\alpha \int_0^{2\pi} \mathrm{d}\gamma \mathbf{X}(e,\alpha,\beta,\gamma), \mathbf{X} = \mathbf{Z}, \mathbf{K}, \tag{24}$$

$$\overline{\overline{\mathbf{X}}}(e) = \frac{1}{\pi} \int_0^\pi \mathrm{d}\beta \, \mathrm{p}(\beta) \overline{\mathbf{X}}(e, \beta), \mathbf{X} = \mathbf{Z}, \mathbf{K}$$

$$\mathrm{p}(\beta) = \sin(\beta) \exp\left(-\frac{\beta}{2\sigma_\beta^2}\right) \qquad \qquad (25)$$

As a complementary note for orientation averaging issues, Eq. (25) gives the integration in the Level A to Level B database conversion tool. The standard deviation of Euler angle, σ_β, can be found in the orientation preference column of Table 1.

It is important to consider particle symmetry in the orientation averaging of Eqs. (24) and (25) to avoid redundant evaluation

435   of $\mathbf{Z}$ and $\mathbf{K}$. For example, in the case of a hexagonal plate with 6-fold azimuthal symmetry and xy-plane reflectance symmetry, $\mathbf{Z}$ and $\mathbf{K}$ only need to be evaluated and averaged over $\alpha \in [0, \pi/6]$ and $\beta \in [0, \pi/2]$.

3.3 Raw Single Scattering Properties: Level A

To improve the accuracy of raindrop modeling, it is essential to consider various effects such as the surface tension, hydrostatic and aerodynamic pressures, and static electric forces. By incorporating these factors, a more accurate representation of raindrop

440   model can be achieved compared to the most commonly used spheroid model. In a study conducted by Chuang and Beard (1990), an equilibrium differential equation was utilized to iteratively determine the shape of a falling raindrop with a given mass, which corresponds to a specific diameter D_{eq}. The obtained results were then fitted to Chebyshev polynomials as shown in Eq. (26). This eqation involves the distance between the raindrop's surface to its mass center, denoted as $\chi(\theta)$, where θ is the zenith angle in spherical coordinates (see Figure 6(d)). To enable practical application, the Chebyshev coefficients

445    $a_n(D_{eq})$ were truncated at the 10th term and provided D_{eq} values ranging from 1 to 9 mm, with increments of 0.5 mm. Therefore, for a given D_{eq} value, the corresponding Chebyshev coefficients can be obtained through interpolation.

$$\chi(\theta) = \frac{D_{eq}}{2}\left[1 + \sum_{i=0}^{10} a_n(D_{eq})\big(1 + \cos(n\theta)\big)\right], \qquad (26)$$

The Chebyshev model of raindrops deviates from xy-plane reflectance symmetry, resulting in a flatter bottom surface compared to the spheroid. Conversely, the top surface of raindrop described by the Chebyshev model is sharper. Note that the

450   disparity between the two models becomes more pronounced with increasing D_{eq}, as shown in Figure 6(a)–(c). It is worth mentioning that larger raindrops are more prone to aerodynamic effects.

Comparing the optical properties of two shapes with significantly different aspect ratios is meaningless. To address this, we defined the aspect ratio of the Chebyshev model in Figure 6(d), which represents the vertical maximum dimension b' versus the horizontal maximum dimension a'. Figure 7 illustrate a comparison between the aspect ratio of the Chebyshev model, as

455   defined above, and the aspect ratio of the commonly used spheroid raindrop model (Thurai et al., 2007; Brandes et al., 2002). It is apparent that for common raindrops with D_{eq}<8 mm, the aspect ratios of the two models are approximately equal.

Therefore, we can confidently assert that the differences in optical properties between the spheroid and Chebyshev models arise from higher-order shape specifications rather than the first-order aspect ratio parameter.
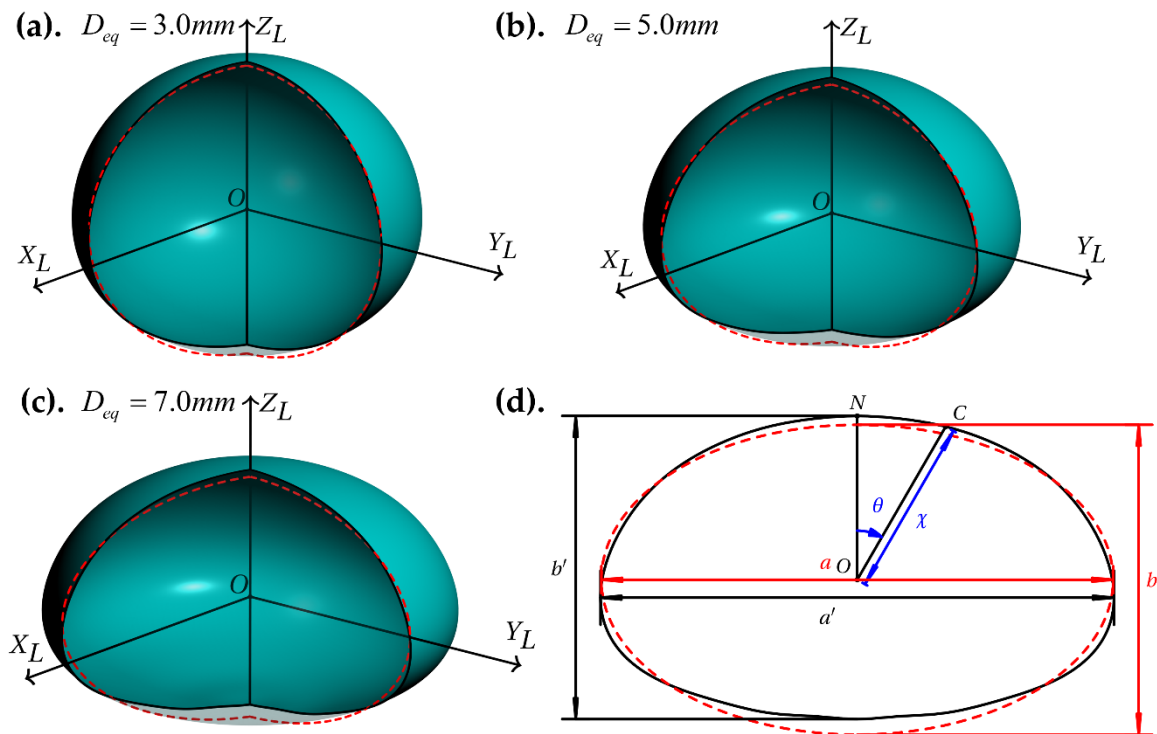

Figure 6: Illustration of raindrops described based on the Chebyshev model. Panels (a), (b), and (c) display the shapes of the Chebyshev raindrop with equal-volume-sphere diameters (D_{eq}) of 3, 5, and 7 mm, respectively. Panel (d) shows the vertical cross-section of the Chebyshev shape corresponding to panel (c), and it also illustrates how the aspect ratio b'/a' is defined for a Chebyshev raindrop. The dashed red lines in all panels show the spheroid model with identical D_{eq} for comparison. The aspect ratio of the spheroid was defined as b/a and b and a are shown in panel (d). The Chebyshev shapes in panels (a)–(c) were set to be partially transparent and displayed in an azimuth angle range [-π/6, π/2].

The initial examination of the optical properties of rain droplets and their sensitivity were conducted by Ekelund et al. (2020) using the Chebyshev model. To compare the radar variables between the spheroid and Chebyshev models, they used a modified version of the EBCM T-matrix code (Mishchenko and Travis, 1994). However, it is important to note that the EBCM may encounter numerical instability issues due to the extremely high imaginary part of refractive indices for liquid water around the K band (10~40 GHz), where the Ku- and Ka-bands are located. To ensure accuracy, consistency amd a user-friendly radar operator interface, this study presents an optical property database of the Chebyshev raindrop model at the Ku- and Ka-bands (13.6 and 35.5 GHz, respectively) using the IITM code (Bi et al., 2013).
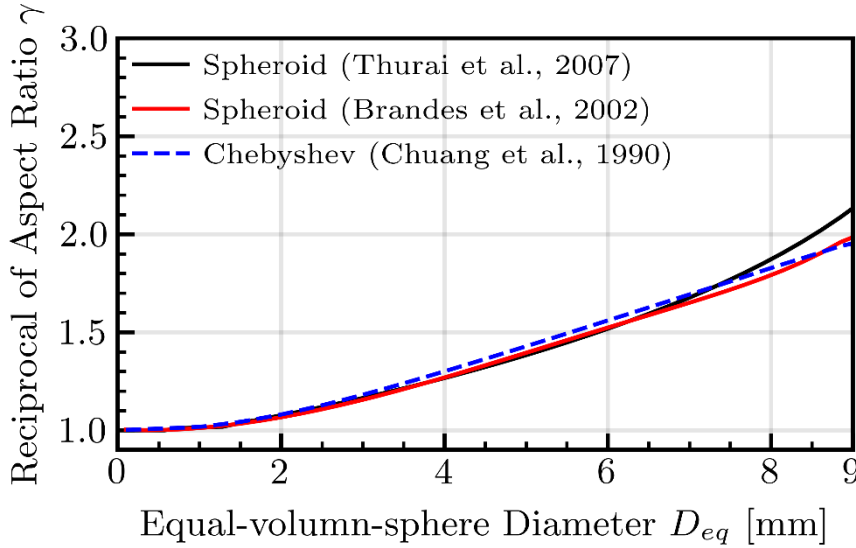
Figure 7: The aspect ratio–diameter relationships as reported in literature. The vertical axis is the reciprocal of the aspect ratio (i.e., γ). Thurai et al. (2007) and Brandes et al. (2002) fitted *in-situ* measurements of two-dimensional video disdrometer (2DVD) measurements by segmented polynomials to give the explicit γ-D_{eq} expressions, while the aspect ratios of the Chebyshev raindrop are estimated with the Chebyshev coefficients recorded by Chuang and Beard (1990) with the method mentioned in Figure 6(d). Since raindrops with their D_{eq} larger than 8 mm disperse easily, the relationships given by Brandes et al. (2002) and Chuang and Beard (1990) end at 9 mm.

To better understand the impact of single-scattering properties on radar variables, it is necessary to visualize the RSSP-Level A database. Additionally, we need to introduce intermediate quantities called the SSP factors for radar variables. The SSP factor $[z_{hv}]$ for the unpolarized reflectivity z_{hv} is defined in Eq. (27), while the SSP factor for unpolarized attenuation $[a_{hv}]$ is defined in Eq. (28). The quantities enclosed in square brackets indicate the SSP factors of the radar variables, while the angle brackets denote the integration over a PSD, often referred to as particle group ensemble mean in certain studies. These factors ($[z_{hv}]$ and $[a_{hv}]$) enable us to assess the contribution of particles with a diameter D_{eq} to the radar reflectivity and specific attenuation, respectively. For further SSP factors for level A database diagnoses, please refer to Figure 10.

$$z_{hv} = \frac{2\lambda^4}{\pi^4 |K_w|^2} \left(\langle Z_{11} \rangle + \langle Z_{22} \rangle \right) = \left\langle [z_{hv}] \right\rangle$$
$$[z_{hv}] = \frac{(Z_{11} + Z_{22}) \cdot (2\lambda^4)}{\pi^4 |K_w|^2}$$

$$\text{(27)}$$

$$a_{hv} = 10^{-3} \cdot \langle K_{11} \rangle = 10^{-3} \cdot \left\langle [a_{hv}] \right\rangle$$
$$[a_{hv}] = K_{11} = \frac{\sigma_{ext,h} + \sigma_{ext,v}}{2}$$

$$\text{(28)}$$
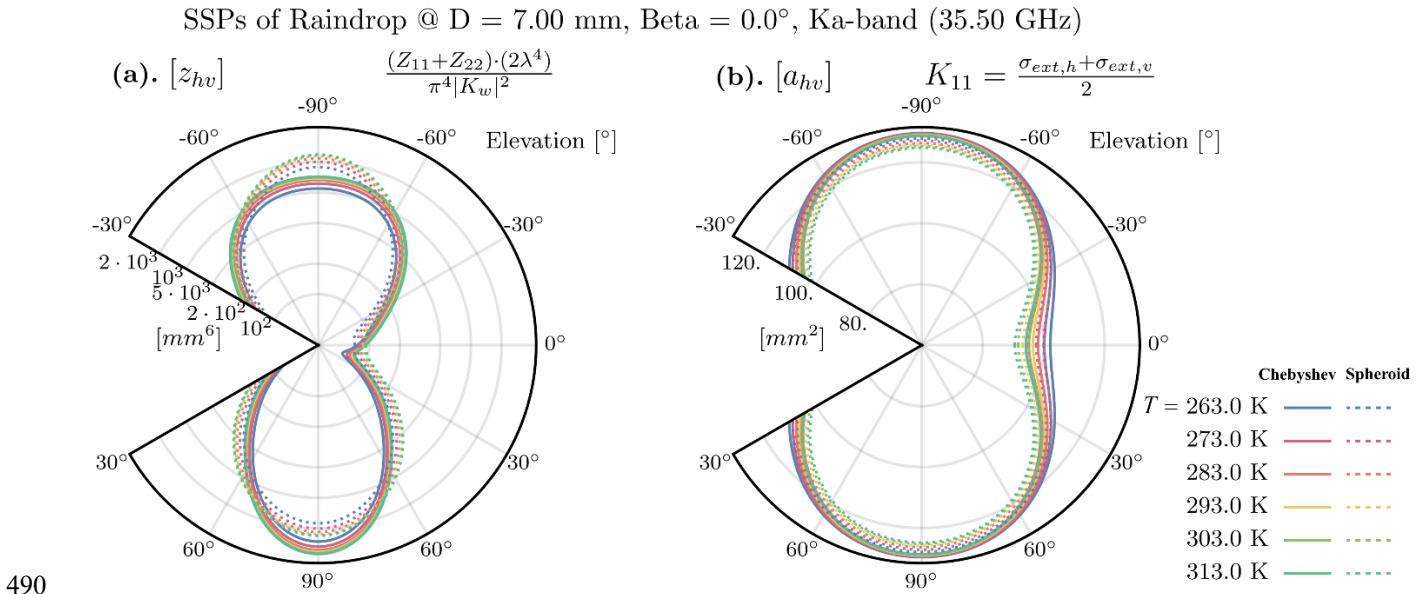
Figure 8: (a). Single-scattering properties (SSP) factor of unpolarized reflectivity and (b). SSP factor of unpolarized attenuation against the elevation angle of radar beam for a raindrop with an equal-volume-sphere diameter of 7.0 mm at the Ka band (35.5 GHz), with their expression in the upper right corner of the panels. The SSP factors of the Level A database are displayed for different temperatures with lines in different colours. The results of the Chebyshev raindrop analysis are indicated with solid lines while those of spheroid raindrop are indicated with dotted lines. The β dimension in the database are fixed at 0°. The negative elevation angles are placed in the upper half circle to indicate the nadir observation geometry of space-borne radar. We masked a sector on the left of each panel to add labels on the radius since such charts absolutely preserve bilateral symmetry.
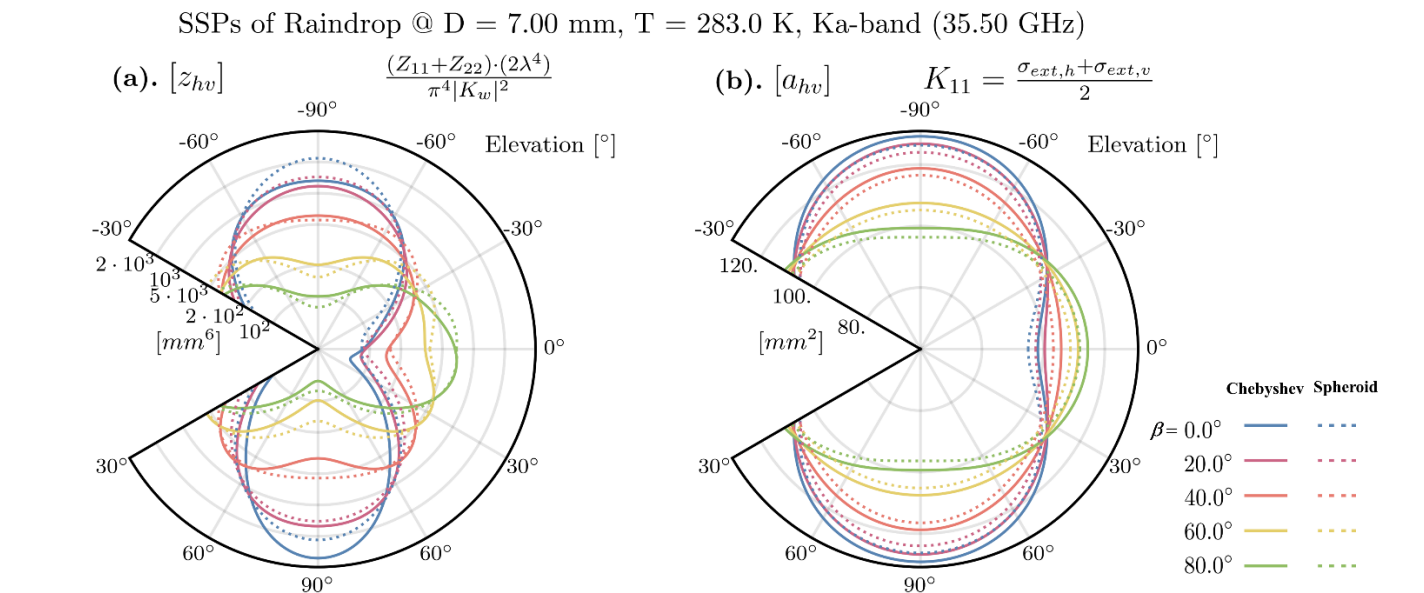
Figure 9: The results for different orientation angles (β) are displayed with different colours in a manner resembling Figure 8. The temperature in the database was fixed at 10 °C (283 K) in this figure.
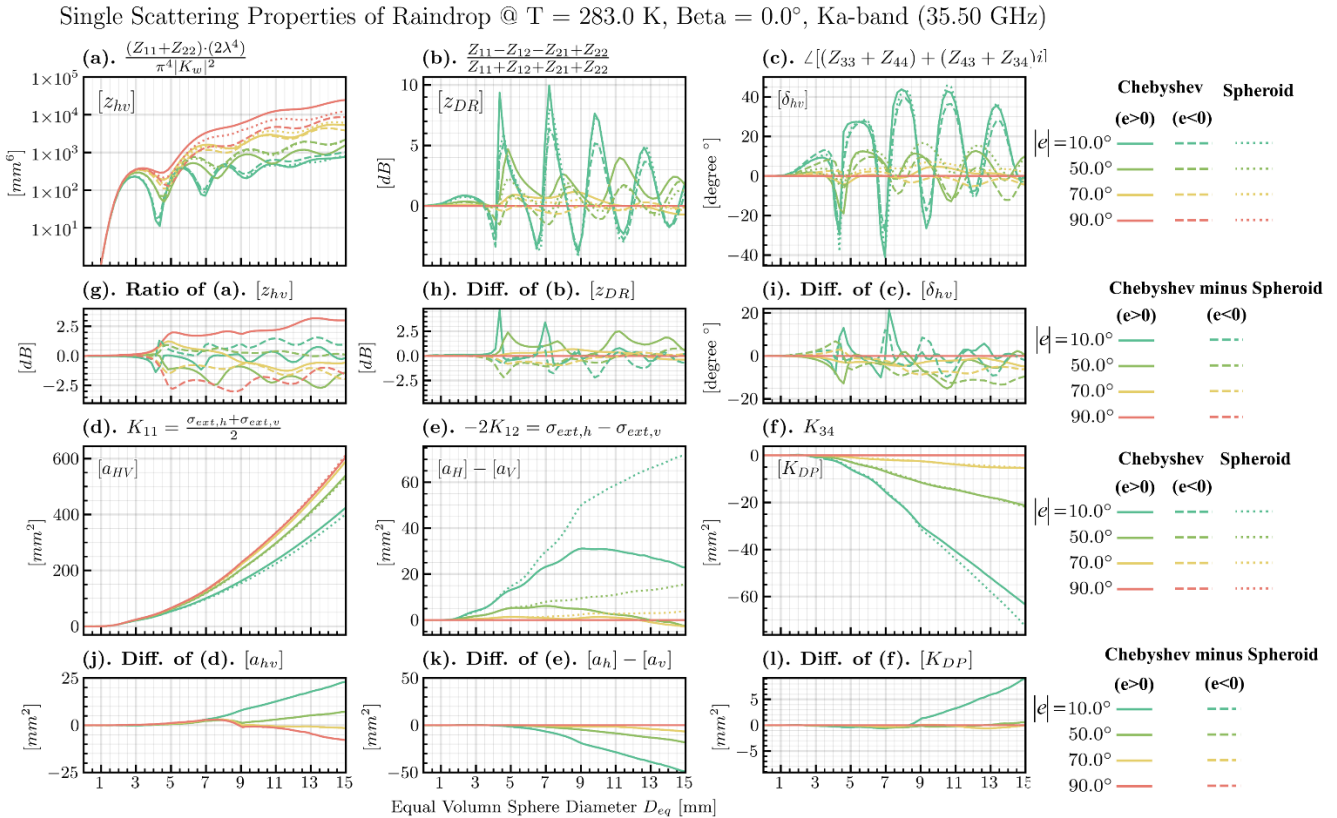
Figure 10: The SSP factors of intrinsic radar variables (indicated in the upper left corner) for the Chebyshev model and the spheroid raindrop models against the equal-volume-diameter of the liquid particles at the Ka band (35.5 GHz) and 283 K. Lines with different colours display the SSP factors for different elevation angles of the radar beam. Results of positive elevation angles for spheroids are indicated by solid lines while those of negative elevation angles are indicated by dashed lines. Since the results of spheroids have xy-plane reflectance symmetry, the negative and positive results are merged as dotted lines. The flatter auxiliary panels (g)–(l) (the second and the fourth rows) below the major panels (a)–(f) (the first and third rows) display the corresponding differences (or ratios) of optical properties beween the Chebyshev model and the spheroid models, respectively. The first column shows unpolarized SSP factors mentioned in Figure 8 and Figure 9, the second column shows SSP factors contributing to observed differential reflectivity, and the third column shows the SSP factors contributing to the observed total phase shift.

It is not surprising to observe that the scattering properties exhibited symmetry with respect to the radar beam elevation angle, e = 0°, for the spheroid model. This is because spheroids possess reflectance symmetry in the xy-plane. However, this symmetry does not hold true for the Chebyshev model. We found that the SSP factor $[z_{hv}]$ had a more pronounced peak than spheroids near the nadir observation geometries (specifically, e = 90°, which is frequently encountered for the vertical-profiling cloud radar), as shown in Figure 8(a). Conversely, the peak near the zenith (namely, e = –90°, for the space-borne radar) was weaker. This phenomenon was also described by Ekelund et al. (2020) for the Chebyshev model at 94.1 GHz, which is likely attributed to its flatter bottom surface and sharper top surface geometries, as depicted in Figure 6. Additionally, we found that the $[z_{hv}]$ factor for ground-based observation geometries (e = 0~20°) was significantly weaker compared to the values obtained

25

for the spheroid model. However, deviations from the spheroid model were typically much smaller for lower frequency bands,
520 such as the Ku band (13.6 GHz) (figure not shown here).

However, the forward scattering properties such as $[a_{hv}]$ of the Chebyshev model still maintain their symmetry with respect to the beam elevation angle e=0°, which can be easily understood based on the reciprocal theory (Van De Hulst, 1981). It is important to note that the attenuation effects of Chebyshev raindrops are slightly stronger compared to spheroid ones.

Figure 8 also demonstrate the stability of the deviations between the Chebyshev model and the spheroid model (CmS hereafter)
525 in terms of the temperature dimension. However, the finding is different for $[z_{hv}]$ against the orientation preference dimension β (see Figure 9a). It was found that the positive and negative CmSs of $[z_{hv}]$ at nadir and zenith, respectively, hold true only if β < 20°. In cases where particle groups have larger canting angles (β > 20°), the CmS for $[z_{hv}]$ can produce a reversal of their signs (Figure 9a). Fortunately, the column "orientation preference" in Table 1 shows that the standard deviation of β = 7° did not exceed this threshold for raindrops.

530 As for $[a_{hv}]$, we learned that the conclusions of CmS at β=0° always hold true when β is sufficiently large (Figure 9b).

We also examined the results across the entire PSD range of raindrops shown in Figure 10. It was found that the aforementioned CmS results for $[z_{hv}]$ were significant when D_{eq} > 3 mm (Figure 10g), while those for $[a_{hv}]$ were significant only for larger raindrops (i.e., D_{eq} > 5 mm, see Figure 10j).

It is worth mentioning that raindrops had significantly higher $[z_{hv}]$ for larger absolute values of the beam elevation angle e
535 (Figure 10a). This can be easily understood since zenith or nadir observation geometries tend to capture a larger cross-section of oblate-spheroid-like models.

3.4 PSD Options and Applied Single Scattering Properties: Level B

The canting angle of raindrops is generally small, so the CmS deviations of SSP factors found in Figure 8 and Figure 10 only show a minor decay when compared to the curves of β = 0°. Hence, there is no need to show the figures for SSP factors again
540 in this section. Instead, we will focus on describing the PSD options for raindrops and the methods used to analyze their impacts on the convertion of SSP factors of radar variables to intrinsic radar variables (namely, ASSP to BSP conversion).

In ZJU-AERO, a total of six options for PSD schemes for raindrops were available, which are listed in Table 3. All schemes were designed for rain modelled by a single-moment microphysics scheme with exponential distribution assumptions. Each PSD schemes can be visualized as a N_0-λ curve, as shown in Figure 11.

545 The constant N_0 parameterization originally proposed by Marshall and Palmer (1948) and used in microphysics packages, such as Hong and Lim (2006), provides a rough approximation for various liquid precipitation scenarios. However, modern PSD schemes for rain, such as the one by Thompson et al. (2008), aim to capture the observed transition from high concentrations

of drizzle-sized drops (D_{eq} < 0.5 mm) in stratocumulus clouds to PSDs dominated by large mm-sized raindrops in heavy precipitation.

550 Among the six schemes, group A is characterized by a power-law N_0-λ relationship, represented as a straight line in the dual-log-scale diagram of Figure 11. On the other hand, the intercept parameter, N_0, for group B schemes follows a formalization described by Eq. (29), transitioning from N_2 to N_1 as the water mass concentration, Q_R, increases. This can be visualized as tanh-like curves shown in Figure 11:

$$N_0 = \left(\frac{N_1 - N_2}{2} \right) \tanh \left[\frac{(Q_{R0} - Q_R)}{4 Q_{R0}} \right] + \left(\frac{N_1 + N_2}{2} \right), \tag{29}$$

555 The values of reference rain water mass concentration Q_{R0} and the dynamic range [N_2, N_1] of the intercept parameter are displayed in the group B of Table 3.

Table 3: The parameters of rain particle size distribution (PSD) schemes available in ZJU-AERO. The group A of PSD schemes: (1) MP1948, (2) AB2012, (3) Walters2011, and (4) Wang2016 can be generalized as a power-law N_0-λ relationship as stated in Section 2.3, while group B of PSD schemes: (1) Thompson2008 and (2) ThompsonTuned can be generalized as Eq. (29), in which N_0 is simply
560 **determined by the mass concentration of rain. The last scheme tagged as "ThompsonTuned" was proposed in the present study to fit of the observations in the case study presented in Section 4. Note that the 10-based or 1000-based coefficients in the "x_1" column of group A are used for unit conversion as the parameters are taken from various studies with divergent unit conventions. Also note that the parameter Q_{R0} is originally a mixing ratio in units of kg·kg^{-1} rather than mass concentration in units of kg·m^{-3}, but we have performed the conversion by assuming ρ_{air}=1.225 kg·m^{-3} of standard atmosphere.**

565 **Group A:**

PSD schemes	Tag	x_1 [mm$^{x_2-1}$·m^{-3}]	x_2 [-]
Marshall and Palmer (1948)	MP1948	8.0×10^3	0.0
Abel and Boutle (2012)	AB2012	$0.22\times1000^{x_2-1}$	2.20
Walters et al. (2011)	Walters2011	$26.2\times1000^{x_2-1}$	1.57
Wang et al. (2016)	Wang2016	14.1×10^{x_2}	1.49

Group B:

PSD schemes	Tag	N_1 [mm^{-1}·m^{-3}]	N_2 [mm^{-1}·m^{-3}]	Q_{R0} [kg·m^{-3}]
Thompson et al. (2008)	Thompson2008	9.0×10^6	2.0×10^3	1.225×10^{-4}
Thompson et al. (2008) Tuned	ThompsonTuned	1.0×10^5	3.0×10^3	3.0×10^{-4}
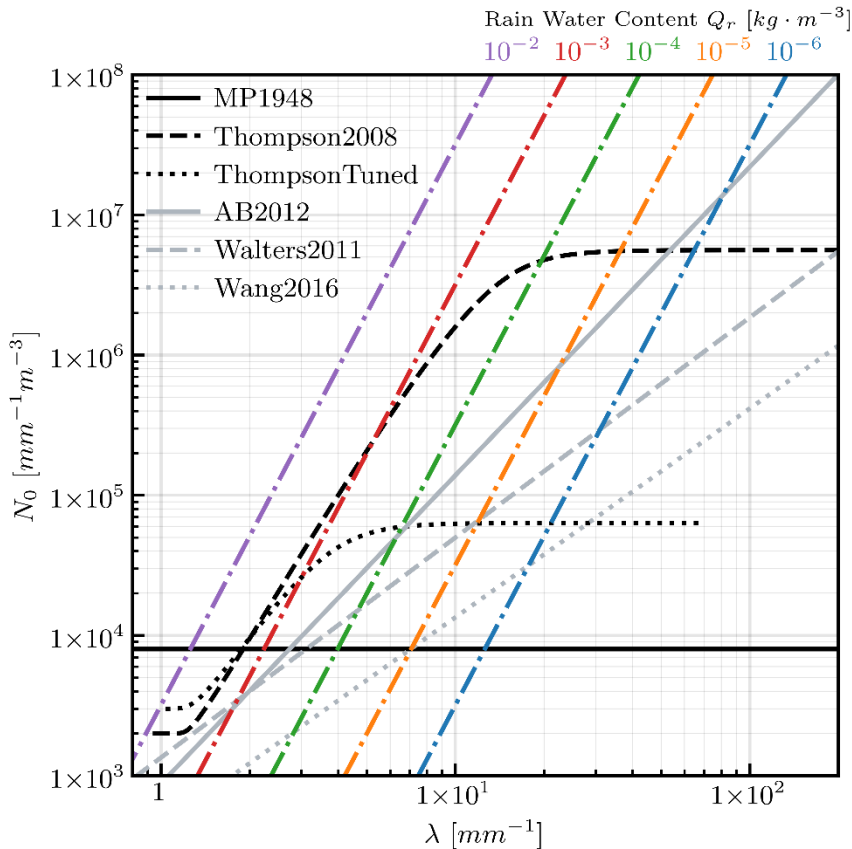
Figure 11: The N_0-λ diagram introduced by Abel and Boutle (2012). All the PSD schemes mentioned in Table 1 are represented as black or grey curves in this figure. The rainbow-coloured dash–dotted lines represent isolines of water concentration for rain Q_R. The curves extend to the upper right corner as Q_R increases. The solution of (N_0, λ) for a given PSD scheme and Q_R can be found by determining the intersection of colored curves and black/gray curves in this diagram.

Obviously, Figure 11 demonstrates that the uncertainty of intercept parameter N_0 varies significantly for different PSD schemes. The Thompson scheme (Thompson et al., 2008) priorities smaller drops, while the Wang scheme (Wang et al., 2016) places more emphasis on larger drops. This diversity in PSDs has important implications for meteorological and microphysics studies. For example, stratocumulus precipitation has less opportunities for collisions, whreas heavier precipitations events, as observed by Wang et al. (2016), experiences stronger updrafts and hence more collisions. Additionally, the strong horizontal and vertical wind shear in the eye-walls of tropical cyclones can lead to the destruction of drops and the production of unusual PSDs (Radhakrishna, 2022), as illustrated in the case study in Section 4.

To explore the effects of different PSD schemes on the radar variables, we introduced the concept of "backscatagrand" and plotted the results for five PSD schemes in Figure 12. The idea of analysing "backscatagrand" was inspired by the definition of "extagrand" used in the analysis of RTTOV-SCATT bulk-scattering tables (Geer et al., 2021), which helps diagnosing the single-particle contribution to extinction coefficients in radiative transfer simulations of passive microwave sounders. The

28

concept of "extagrand" was based on the insight that the total extinction of an emsemble of particles is primarily influenced

by a fraction of particles within a narrow diameter range. Therefore, by analyzing the SSP for particles within that size range,

585   we can infer the BSP of the entire ensemble of particles. The "extagrand" $\sigma_{ext}(D)N(D)$ in units of $mm \cdot m^{-3}$ was factorized as

the product of mass distributions $m(D)N(D)$ in units of $kg \cdot mm^{-1} \cdot m^{-3}$ and the extinction cross section per unit volume

$\sigma_{ext}(D)/m(D)$ in units of $mm^2 \cdot kg^{-1}$. These quantities are determined by PSDs and SSPs, respectively. The "extagrand" quantities

are appreciable only for size ranges in which both mass distribution $m(D)N(D)$ and mass extinction efficiency $\sigma_{ext}(D)/m(D)$

are large enough to produce significant products "extagrand".

590   However, for weather radar applications, the principal quantity is backscattering rather than the extinction, as is the case for

passive instruments. Hence, we have introduced parallel definitions of the unpolarized backscattering cross section per volume

$\sigma_{bsca,hv}(D)/m(D)$, which we referr to as mass backscattering efficiency hereafter and the "backscatagrand" $\sigma_{bsca,hv}(D)N(D)$ in

which $\sigma_{bsca,hv}(D)$ indicates the unpolarized backscattering cross section defined as $\sigma_{bsca,hv} = \left(\sigma_{bsca,h} + \sigma_{bsca,v} \right)/2 = 4\pi(Z_{11} + Z_{22})$.
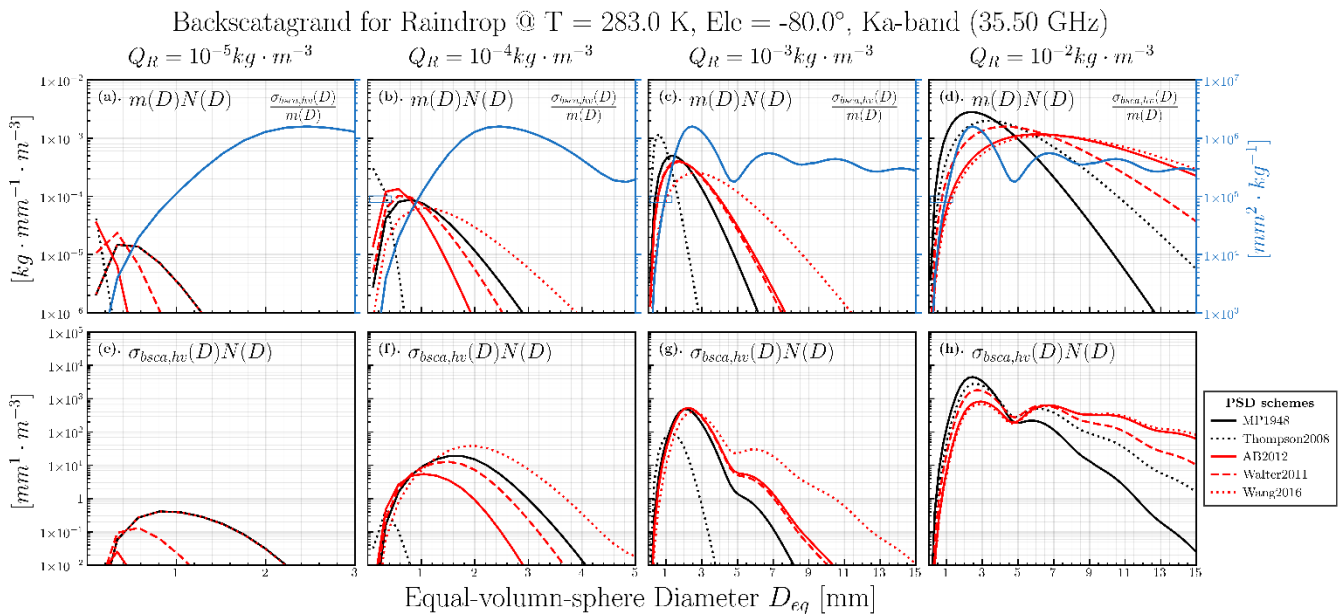

Figure 12: The analysis of the integration of single particle unpolarized backscattering over the PSD. The unpolarized backscattering cross section $\sigma_{bsca,hv}$ was obtained using the applied single scattering properties (ASSP) – Level B of the Chebyshev raindrop database. The regular conditions of space-borne radar (T = 283 K, e = –80°) at the Ka band (35.5 GHz) (indicated in the title) were considered. The first row displays the mass distribution $m(D)N(D)$ for five PSD schemes and four water concentration settings, while the single-particle unpolarized backscattering per unit particle mass $\sigma_{bsca,hv}(D)/m(D)$ is indicated by the blue lines with the blue axis and labels marked on the right. The second row shows the quantity "backscatagrand" $\sigma_{bsca,hv}(D)N(D)$ for different PSD schemes and water concentrations, which is a measure of contributions particles make to the total reflectivity z_{hv} (the principal intrinsic radar variable). Readers can verify that the red or black curves in the first row multiplied by the blue curve exactly yield the second row's curves.

It can be concluded from Figure 12 that the mass distributions and backscattering contribution spectrum (i.e., the so-called

605   "backscatagrand") exhibit large uncertainties due to different PSD schemes. The mass backscattering efficiency has multiple

oscillations caused by the resonance effect, particularly in high-frequency bands such as the Ka-band. Specifically, two important peaks of mass backscattering efficiency at D_{eq} = 2.5 mm and D_{eq} = 6.5 mm and one important dip at D_{eq}=5.0 mm exist (solid blue line in Figure 12(d)). For extremely heavy precipitations ($Q_R \sim 10^{-2}$ kg·m^{-3}), the peak of mass distributions might coincide with the dip of mass backscattering efficiency at D_{eq}=5.0 mm. This phenomenon is unique to modern PSD

610   schemes (such as Wang2016 and AB2012), which priorities larger drops for heavy rain, leading to a loss of bulk reflectivity if the total mass of raindrop remains constant.

Under moderately heavy precipitation conditions ($Q_R \sim 10^{-3}$ kg·m^{-3}, see Figure 12c&g), the Thompson2008 PSD scheme stands out as an outlier. Its extremely large N_0 compared to other schemes (see Figure 11) leads to an significantly smaller peak in mass distributions as small as D_{eq} < 1.0 mm, enven though the peak of other PSD schemes is approaching the first peak of

615   mass backscattering efficiency at D_{eq} = 2.5 mm. Accordingly, the total reflectivity computed with the Thompson2008 scheme must be much smaller at Q_R=10^{-3} kg·m^{-3} than those computed with other PSDs.

The relative importance of particles in the entire spectrum can also be diagnosed with the curves of backscatagrand. For example, we can learn from Figure 12h that the contribution of backscattering is dominated by particles with diameter D_{eq} at around 2.5 mm for the MP1948 scheme, while the contribution from particles of 2.5 mm-size and 6.5 mm-size are almost

620   equally important for the Wang2016 and AB2012 schemes. To go further, we can infer that the CmS deviations mentioned in Section 3.3 can only affect the bulk-scattering properties computed with the Wang2016 and AB2012 schemes, since the CmS deviations of backscattering are only significant for particles with D_{eq}>3 mm (Figure 10g).

3.5 Bulk Scattering Properties: Level C

Figure 13 shows the intrinsic radar variables for the Chebyshev model, which were computed using the BSP database and

625   the spheroid model at the Ka band. In Section 3.4, we made speculations based on the backscatagrand plot, and we can now confirm these speculations individually:

1.   The application of PSD schemes, such as Wang2016, can result in a significant reduction in the reflectivity Z_{hv} (by approximately 5 dBZ) for extremely heavy precipitation scenarios compared to the default PSD scheme MP1948 (refer to Figure 13a, $Q_R \sim 10^{-2}$ kg·m^{-3}).

630   2.   The reflectivity Z_{hv} computed by the Thompson2008 scheme for moderately heavy precipitation scenarios is considerably lower (by over 10 dBZ) compared to other PSD schemes in group A of Table 1 (refer to Figure 13a, $Q_R \sim 10^{-3}$ kg·m^{-3}).

3.   The CmS deviations are only significant (reducing Z_{hv} by about 2 dBZ) for extremely heavy precipitation scenarios and PSD schemes that emphasize larger drops, such as Wang2016 (refer to Figure 13a, $Q_R \sim 10^{-2}$ kg·m^{-3}).

635   4.   The CmS deviations of attenuations, a_{hv}, are never significant for regular mass concentrations of rain Q_R (see Figure 13d), This finding can be explained by the fact that the CmS deviations in RSSP (Figure 10j) are significant only if

D_{eq} > 7 mm, which represents a group of drops sharing a small fraction of the mass distribution, even for extremely
heavy precipitations.

640 From Figure 13, it can be concluded that the unpolarized intrinsic radar variables Z_{hv} and a_{hv} at the Ka band (actually also for
the Ku band, not shown here) are more sensitive to the uncertainty of PSD schemes than the CmS optical properties
deviations for space-borne radar observation geometries. The CmS deviations are only notable for extremely heavy
precipitation scenarios in which large drops are prominent. However, the sensitivities of polarimetric intrinsic radar variables
with respect to CmS deviations for ground-based radars and geometries were not examined in this paper.
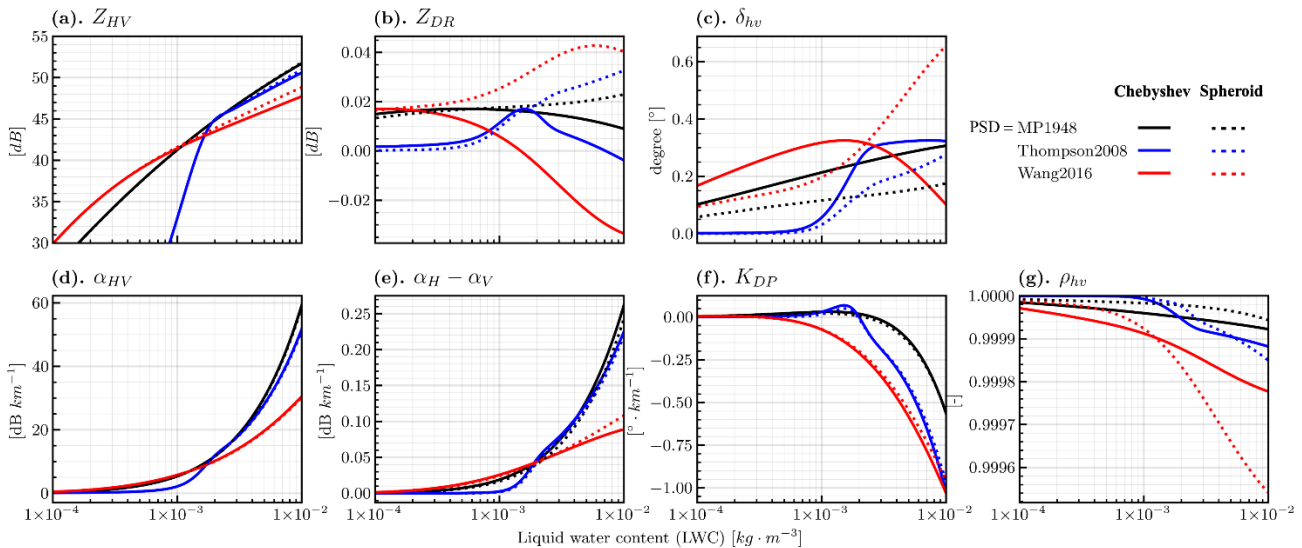
645 **Figure 13: The intrinsic radar variables against the liquid water content (mass concentration of rain Q_R) computed with the bulk
scattering properties (BSP) Level C database of the Chebyshev raindrop and spheroid models, which were indicated by solid and
dotted curves, respectively. A typical condition of the space-borne radar (T = 283 K, e = −80°) at the Ka band (35.5 GHz) was
considered. The panels (a)–(f) display the six intrinsic radar variables that can be diagnosed from the corresponding factors of SSP
in Figure 10(a)–(f), placed with the same arrangement. Note that a new panel (g) for cross-polar correlation coefficient ρ_{hv} was
650 added, since ρ_{hv} characterized the consistency of polarimetric optical properties across the ensemble of particles and therefore had
no corresponding SSP factors. The colors of the curves are used to indicate three typical PSD schemes chosen from Table 1.**

4 Case Studies

To assess the simulation capabilities of ZJU-AERO, we conducted case studies using the real-world data and investigated the
sensitivities of the PSD schemes and the new Chebyshev raindrop model. For this study, we chose the GPM core satellite
655 (referred to as GPM hereafter) and specifically analyzed the overpass of Typhoon Haishen, the first super typhoon of the 2020
Northwest Pacific typhoon season, on September 5, 2020, at 09:21UTC. We used the simulation and observation data from
the dual-frequency precipitation radar (DPR) onboard the GPM for our analysis.

To conduct the ZJU-AERO simulations, we utilized model grid data generated by the operational run of CMA-MESO, which
was initialized at 00 UTC of September 5, 2020. The CMA-MESO grid data had a horizontal resolution of 3 km and consisted

660   of 50 vertical layers. Note that the WSM6 microphysics package was selected for the CMA-MESO operational run. However, any forced PSD schemes could be applied in the simulation of the radar operator, as mentioned in Section 2.3.

4.1 Simulation of a Tropical Cyclone Case

According to Iguchi et al. (2003), the GPM-DPR's Ku-band radar is similar to the Tropical Rainfall Measurement Mission (TRMM) Precipitation Radar (PR), while the Ka-band radar is sensitive to light rain and snow. By combining data from two

665   channels, accurate estimates of drop size distribution (DSD) parameters can be obtained. The Ka-band radar has two modes (Iguchi et al., 2010): (1) a high-sensitivity mode for light-rain and snow (high-sensitivity beam) and (2) a matched-beam mode in which the sampling volumes of Ka- and Ku-band radar are collocated (matched beam). However, since May 21, 2018, the GPM-DPR has switched its scan pattern, and now a full swath can be considered as the matched beam. Therefore, in this case study, we used data from the Ka-band in the matched-beam mode to estimate DSD and drop morphology parameters.

670   The dual frequency ratio (DFR) is defined as the difference between the measured reflectivity at two channels (Ku- and Ka-bands). Previous studies have shown that the DFR can be used to distinguish between stratiform and convective rain (Le and Chandrasekar, 2012).

Figure 14 displays the observation and simulation of the Ku-band radar reflectivity at different levels, with the last row showing the mismatch between them (i.e., the OmB of reflectivity). Figure 15 presents the cross-section of radar reflectivity between

675   points A and B in Figure 14, separately for the Ku- and Ka-bands. Additionally, the last column shows the DFR as defined above. Based on the comparison between observations and simulations in Figure 14 and Figure 15, it can be concluded that the regional model of CMA-MESO is able to capture some of storm structures, such as the cyclone eye and eye-wall. However, the structures of outer spiral rain bands in the simulation (Figure 14e and Figure 15d) are described as contiguous and vague, rather than the isolated towering bands depicted by the GPM-DPR measurements (Figure 14a and Figure 15a). Although the

680   NWP model could not accurately predict the cloud and precipitation timing and position, the possibility distribution of simulated radar reflectivity should be unbiased when compared with observations; otherwise, a systematic bias in the NWP model or the radar operator might be identified. In this case, we assume that the NWP model CMA-MESO was roughly unbiased.

Notably, the freezing level in this case was found within the altitudes ranging from 4 to 5 km (the temperature profile of

685   model is not shown here), which is believed to contain abundant melting particles. Actually, the GPM-DPR observations revealed a prominant bright band (BB) in this melting layer (Figure 15a and b). It's worth noting that long-term radar observations of melting layers of precipitation and their interpretations were previously documented by Fabry and Zawadzki (1995). However, the simulations we conducted did not show an obvious bright BB, which was attributed to the absence of a representationof melting particles in ZJU-AERO. Based on the observations and simulations, it was expected that the

690   melting layer would exhibit have a positive OmB signature. However,in Figure 15g and h, we encountered difficulties in identifying continuous positive mean bias of the OmB for both the Ku- and Ka-bands in the melting layer. This challenge

arose due to the large mislocation errors of precipitation predicted by the NWP model used in this study. To address this issue, future analysis could employ horizontal averaging or examine the probability distribution function of reflectivities in the melting layer. We plan to report on melting particle models and their relevant validations in upcoming publications.
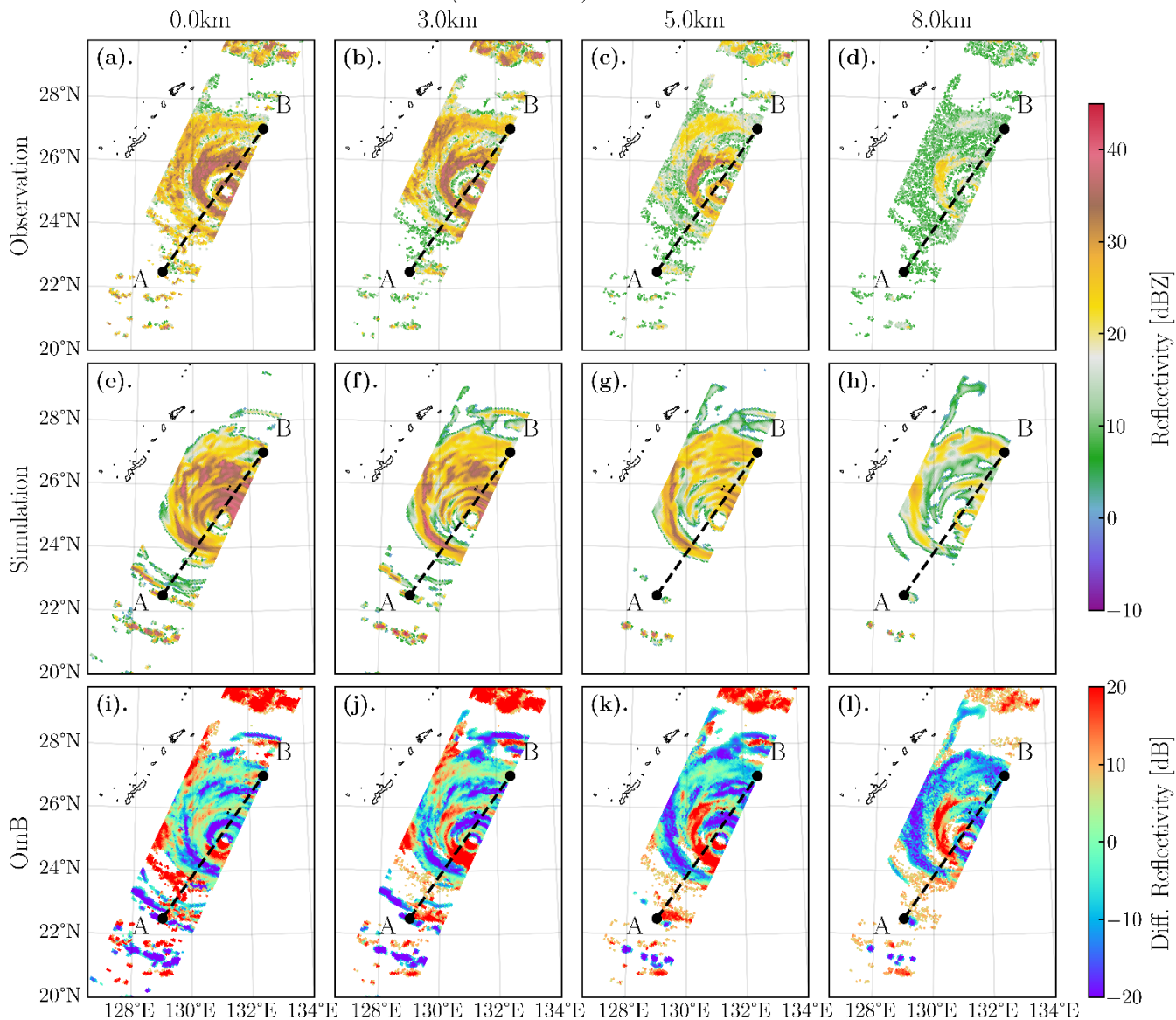
Figure 14: Panels (a)-(d) display the Global Precipitation Mission-Dual Frequency Precipitation Radar (GPM-DPR) observed radar reflectivity at the Ku band (13.6 GHz) for the overpass of Typhoon Haishen at 09:21 UTC on September 5, 2020. The results shown at different columns corresponds to four altitude levels (namely, 0, 3, 5, and 8 km). The second row (panels e–h) shows the simulated radar reflectivity by applying the output of the CMA-MESO to the ZJU-AERO. The last row (panels i–l) shows the observation minus simulation (OmB) of radar reflectivity of the four levels. The radar gates for which the reflectivity is below the sensitivity of space-borne radar are filled with a "background" reflectivity of 0 dB to generate the OmB reflectivity. The reflectivities in panels

a–d are masked by a flag called "flagPrecip" (available at the ground) offered in the L2A swath data of GPM-DPR, while the simulation of reflectivity in panels e–h is masked by the sensitivity threshold of 12 dBZ to keep it the same with sensitivity of GPM/DPR observation. The radar operator applied the ThompsonTuned PSD (see Table 3) option and the Chebyshev morphology
705 **options for the category rain in the simulations. The cross section indicated by the dashed line between A (129°E 22.5°N) and B (132.5°E 27°N) was selected for further studies as shown in Figure 15.**
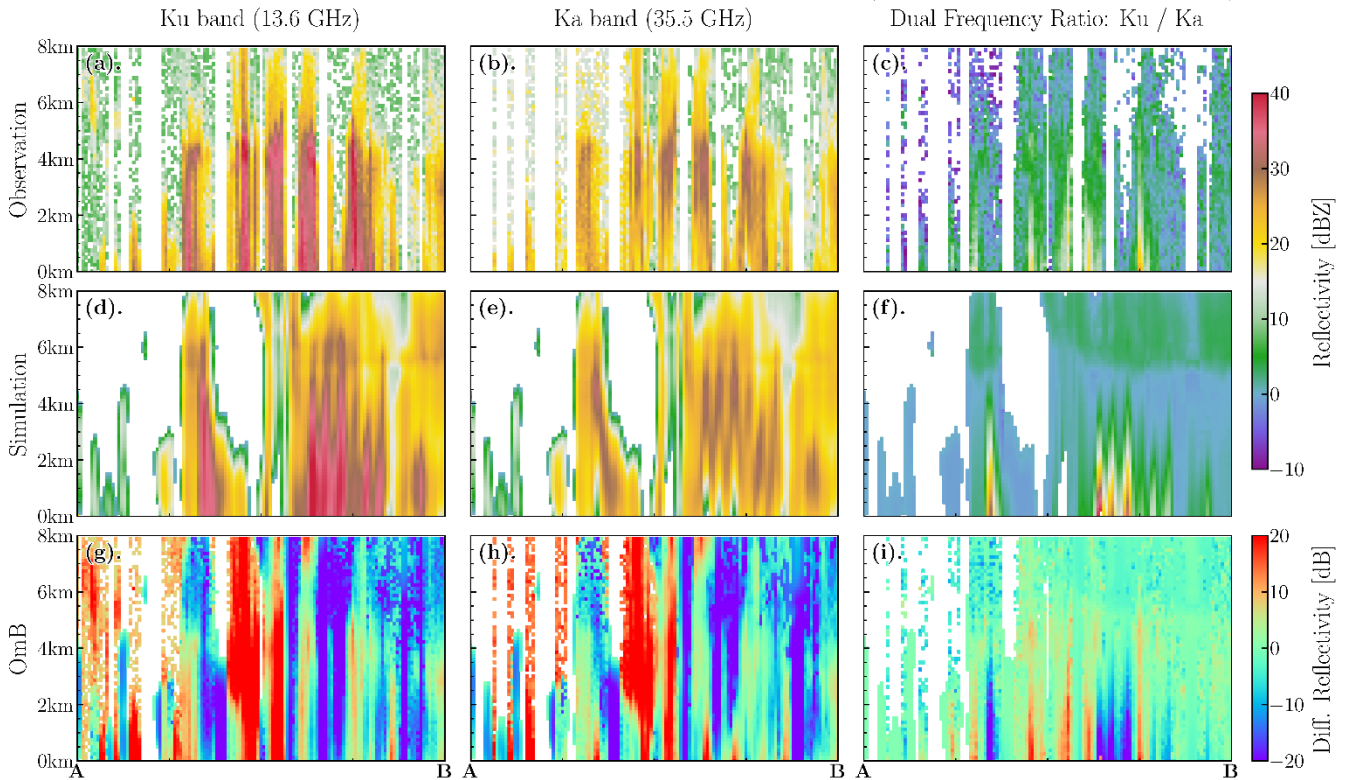
Figure 15: The cross-section of radar reflectivity, indicated by the line AB in Figure 14. The GPM-DPR observations are shown in the first row (panels (a)–(c)), simulations of the radar operator are shown in the second row (panels (d)–(f)), while the OmB of
710 **reflectivity is shown in the third row (panels (g)–(i)). As for the arrangement of panels in column-view, the first, second, and third columns display the results of the Ka and Ku bands and the dual-frequency ratio (DFR, Ku/Ka), respectively. The radar operator applied the ThompsonTuned PSD (see Table 3) and Chebyshev morphology options for the rain category in the simulations.**

Moreover, a minor negative OmB bias was observed for DFR in the 0 to 2 km layer (Figure 15i), which could be attributed to the over-attenuation in the Ka-band simulation (Figure 15e). This speculation is supported by two facts: (1) many weak
715 reflectivity (~10 dBZ) regions are found right beneath the strong reflectivity gates aloft at around 4 km for the Ka band (Figure 15e) and (2) the weak reflectivity regions of the Ka band collocate with the strong reflectivity region (~40 dBZ) of the Ku band (Figure 15d).

The OmB plots, as shown in Figure 14 and Figure 15, are useful tools for verifying and calibrating new observation operators and identifying their deficiencies. Overall, the bias of distributions is reasonable and demonstrates the capability of ZJU-AERO
720 in simulating the reflectivity of dual-frequency spaceborne radar such as GPM-DPR.

4.2 Sensitivity Assessments on Hydrometeor PSDs and Morphologies
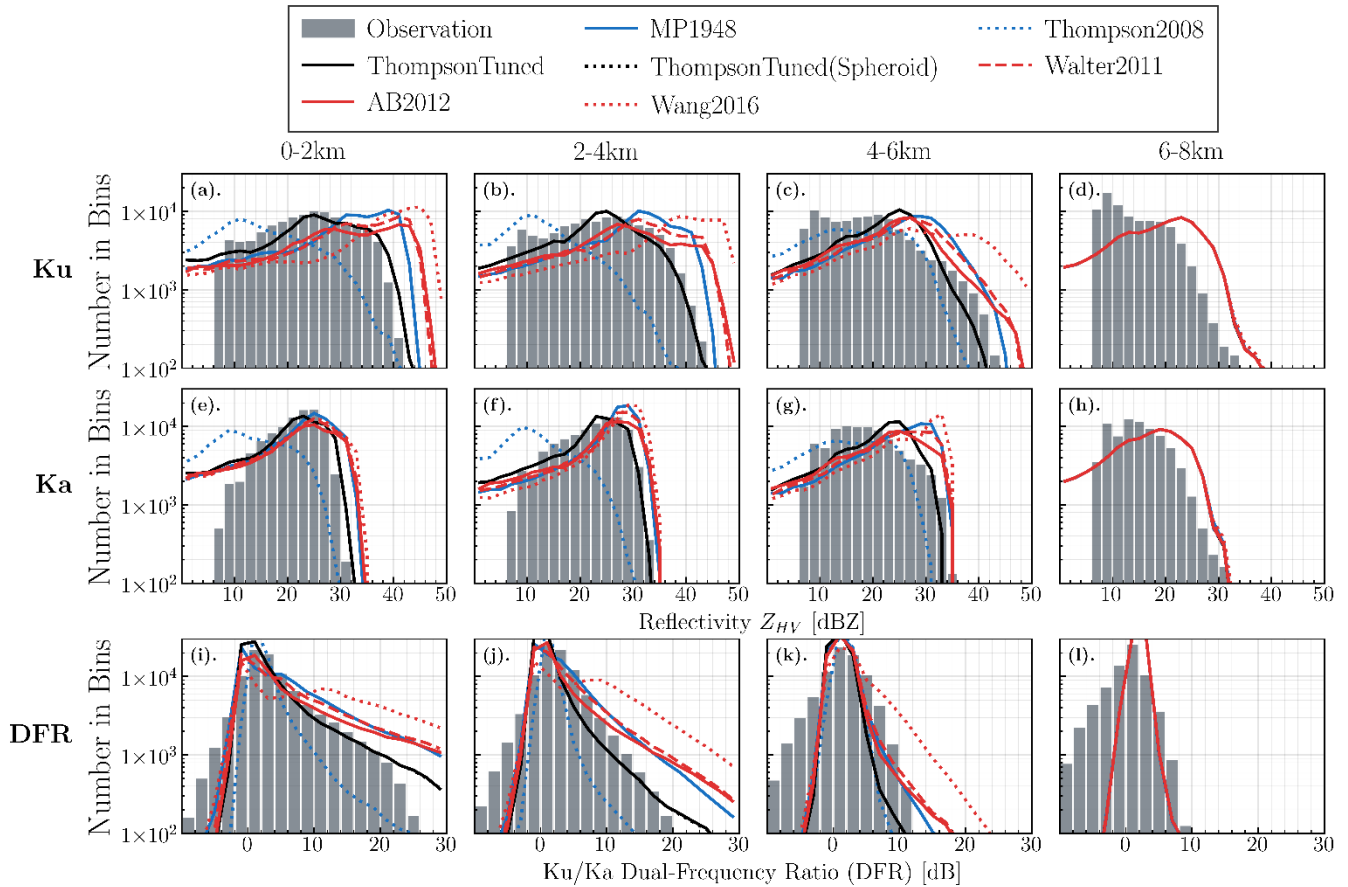
Figure 16: The observation and simulation distributions of radar reflectivity at the Ka (the first row) and Ku (the second row) bands and the dual frequency ratio (DFR) (the third row). The data of distributions were gathered from the reflectivity of all the radar gates in the four altitude layers (namely, the 0–2 km layer, 2–4 km layer, 4–6 km layer, and 6–8 km layers as the tags on the top of the columns suggest). The first two layers (0–2 and 2–4 km) were primarily composed of liquid hydrometeors while the last layer (6–8 km) was a pure solid hydrometeors layer. The intermediate 4–6 km layer is assumed to have melting particles as it contained the freezing level in the CMA-MESO simulation (temperature profiles of the NWP model are not shown here). The observation distributions of reflectivity are shown by grey bars in the panels, while the simulation distributions are indicated by curves with different colours and styles. The radar operator applied the Chebyshev morphology in all the simulations except the group with the label of "ThompsonTuned(Spheroid)", which was simulated with the spheroid raindrop option.

We also performed sensitivity assessments for the PSD and non-spherical morphology options of the rain hydrometeor category. Figure 16 shows the observation and simulation distributions of radar reflectivity at the Ku- and Ka-bands and the dual frequency ratio (DFR) at four altitude layers (0-2 km, 2-4 km, 4-6 km, and 6-8 km). Since we were tuning the liquid hydrometeor, the melting and solid layer in the last two columns (4-6 km and 6-8 km) did not concern us.

Based on statistical analysis, we found that the mass concentration of rain in the CMA-MESO at the storm rain bands was primarily dominated by moderately heavy rain ($Q_R \sim 10^{-3}$ kg·m^{-3}) rather than extremely heavy rain ($Q_R \sim 10^{-2}$ kg·m^{-3}). As a result,

applying the Thompson2008 PSD could lead to a significant reduction in the simulated reflectivity (Figure 13), which is consistent with our findings in Figure 16(a), (b), (e), and (f) for the Ku- and Ka-bands of liquid layers.

740 Due to the strong wind shear in the rain bands of tropical cyclone, large drops can be broken apart (Radhakrishna, 2022), causing the rain PSD in such conditions to behave irregularly and deviate from the prevailing parameterizations. Figure 16(a), (b), (e), and (f) demonstrate that almost all the PSD schemes significantly overestimated the reflectivity for both Ku- and Ka-bands, except for the Thompson2008 scheme, which underestimated the reflectivity.

To address the discrepancy, we designed a new PSD scheme, referred to as the ThompsonTuned, by tuning the parameters in

745 Eq. (29). Fortunately, we identified an optimal point at which the black lines in Figure 16(a), (b), (e), and (f) closely matched the observed distributions. The parameters are listed in Table 3 and plotted in the N_0-λ diagram of Figure 11. The tuned PSD scheme is reasonable as it falls between the MP1948 and Thompson2008 schemes in the N_0-λ diagram, with an emphasis on smaller particles compared to MP1948. This may be attributed to the unusual DSD in tropical cyclones.

While no *in-situ* DSD observations are available to support the tuned PSD schemes used in this study, the implications of the

750 tuning experiments are interesting, considering that the matched-beam observation of Ku and Ka bands were designed for the DSD estimation.

Not surprisingly, the CmS effects were negligible in this case, as it is difficult to discriminate the solid and dashed black lines in Figure 16. This is likely due to the moderately heavy rainfall in tropical cyclones with strong winds, which prevent the large drops from highlighting the CmS deviations. However, we still believe that the CmS effects could be significant in cases of

755 extremely heavy rain in the supercell storms.

5 Summary and Ongoing Tasks

In summary, Section 2 of our study introduced the basic concepts of design in the ZJU-AERO. These concepts included the general procedure, radar variable calculations, and the available hydrometeor settings. We also highlighted the unique features of ZJU-AERO, such as its multi-layered design for the optical database of non-spherical particles. Additionally, we

760 demonstrated the data analysis tools in each layer using the example of the Chebyshev raindrop. Furthermore, we validated the capability of ZJU-AERO by analyzing a case study of a tropical cyclone using input from the CMA-MESO for simulating spaceborne radar observations. We also conducted sensitivity assessments of PSDs and morphology options in ZJU-AERO.

Overall, the results were satisfactory, and the ZJU-AERO operator is ready for experimental and operational usage. However, several aspects of ZJU-AERO still need improvement, and we have listed the ongoing development tasks as follows:

765 1. Improve the geometric characterization and parameterization of melting particles (including melting snow, melting graupel and melting hail) by using layered inhomogeneous modelling rather than an effective medium approximation for the the mixture matrix.

2. Compute the optical properties of melting particles using the IITM code and extend the SSP/BSP database with a new dimension of water fraction.

770 3. Develop more concrete models for single-crystal, aggregated, and rimmed snow to replace the "soft spheroid" model and create a corresponding SSP/BSP database.

 4. Model hail as non-spheroid and inhomogeneous particles.

 5. Include cloud ice, which plays an significant role in the high-frequency bands of spaceborne radar.

 6. Conduct more case studies, particularly with measurements from the spacebore radar FY3-RM-PMR. Notably, the L1
775 product of spaceborne radar FY3-RM-PMR has been accessible online (released by National Satellite Meteorological Center (NSMC) on November 22, 2023) after the manuscript of this paper is finished. We have already implemented modules to interface with the data format of FY3-RM/PMR in ZJU-AERO, but the time coverage of observation data is too limited for us to find a good demonstration case. Therefore, more case studies and fine-tuning should be conduceted with future measurements from FY3RM-PMR.

780 In conclusion, ZJU-AERO is an observation operator that facilitates the exploitation of measurement data from both space-borne and ground-based radars. Its versatility and effectiveness make it a valuable tool for data assimilation in CMA-GFS/MESO. Moreover, ZJU-AERO has the potential to be applied in various other studies within a wide range of contexts.

Acknowledgements

Code Availability

Codes of the forward radar operator ZJU-AERO V0.5 and the packaged Conda environment and the user manual are available
790 on ZENODO (https://doi.org/10.5281/zenodo.10069598). The database of scattering properties (i.e., the LUTs) are also released with the software package.

Data Availability

Two cases of this forward radar operator are presented in the user manual of ZJU-AERO for the demonstration purposes of its usage for the space-borne and ground-based radar, respectively. The NWP model grid data and the radar observation products
795 for those two demonstration cases are also available on ZENODO (https://doi.org/10.5281/zenodo.10058324).

Author Contribution

Hejun Xie performed the coding, visualization of the LUTs, and designed the case study experiments. Lei Bi and Wei Han supervised this study. All authors contributed to the writing of the paper.

Competing Interests

800   The contact author has declared that none of the authors has any competing interests.

References

Abel, S. and Boutle, I.: An improved representation of the raindrop size distribution for single-moment microphysics schemes, Quarterly Journal of the Royal Meteorological Society, 138, 2151-2162, 2012.

805 Bi, L. and Yang, P.: Accurate simulation of the optical properties of atmospheric ice crystals with the invariant imbedding T-matrix method, Journal of Quantitative Spectroscopy and Radiative Transfer, 138, 17-35, 2014.

Bi, L., Yang, P., Kattawar, G. W., and Mishchenko, M. I.: Efficient implementation of the invariant imbedding T-matrix method and the separation of variables method applied to large nonspherical inhomogeneous particles, Journal of Quantitative Spectroscopy and Radiative Transfer, 116, 169-183, 2013.

810 Bi, L., Wang, Z., Han, W., Li, W., and Zhang, X.: Computation of optical properties of core-shell super-spheroids using a GPU implementation of the invariant imbedding T-matrix method, Frontiers in Remote Sensing, 3, 35, 2022.

Brandes, E. A., Zhang, G., and Vivekanandan, J.: Experiments in rainfall estimation with a polarimetric radar in a subtropical environment, Journal of Applied Meteorology, 41, 674-685, 2002.

Chandrasekar, V.: Polarimetric Doppler weather radar [electronic resource]: principles and applications, Cambridge University
815 Press2001.

Chen, D., Xue, J., Yang, X., Zhang, H., Shen, X., Hu, J., Wang, Y., Ji, L., and Chen, J.: New generation of multi-scale NWP system (GRAPES): general scientific design, Chinese Science Bulletin, 53, 3433-3445, 10.1007/s11434-008-0494-z, 2008.

Chuang, C. C. and Beard, K. V.: A numerical model for the equilibrium shape of electrified raindrops, Journal of the atmospheric sciences, 47, 1374-1389, 1990.

820 Ekelund, R., Eriksson, P., and Kahnert, M.: Microwave single-scattering properties of non-spheroidal raindrops, Atmospheric Measurement Techniques, 13, 6933-6944, 2020.

Ellison, W.: Permittivity of pure water, at standard atmospheric pressure, over the frequency range 0–25 THz and the temperature range 0–100 C, Journal of physical and chemical reference data, 36, 1-18, 2007.

Fabry, F. and Zawadzki, I.: Long-term radar observations of the melting layer of precipitation and their interpretation, Journal
825 of the atmospheric sciences, 52, 838-851, 1995.

Field, P., Hogan, R., Brown, P., Illingworth, A., Choularton, T., and Cotton, R.: Parametrization of ice-particle size distributions for mid-latitude stratiform cloud, Quarterly Journal of the Royal Meteorological Society: A journal of the atmospheric sciences, applied meteorology and physical oceanography, 131, 1997-2017, 2005.

Garrett, T., Fallgatter, C., Shkurko, K., and Howlett, D.: Fall speed measurement and high-resolution multi-angle photography
830 of hydrometeors in free fall, Atmos. Meas. Tech, 5, 2625-2633, 2012.

Garrett, T. J., Yuter, S. E., Fallgatter, C., Shkurko, K., Rhodes, S. R., and Endries, J. L.: Orientations and aspect ratios of falling snow, Geophysical Research Letters, 42, 4617-4622, 2015.

Geer, A. J., Bauer, P., Lonitz, K., Barlakas, V., Eriksson, P., Mendrok, J., Doherty, A., Hocking, J., and Chambon, P.: Bulk hydrometeor optical properties for microwave and sub-mm radiative transfer in RTTOV-SCATT v13. 0, Geoscientific Model

835 Development Discussions, 2021, 1-45, 2021.

Hong, S.-Y. and Lim, J.-O. J.: The WRF single-moment 6-class microphysics scheme (WSM6), Asia-Pacific Journal of Atmospheric Sciences, 42, 129-151, 2006.

Hubbert, J., Ellis, S., Dixon, M., and Meymaris, G.: Modeling, error analysis, and evaluation of dual-polarization variables obtained from simultaneous horizontal and vertical polarization transmit radar. Part I: Modeling and antenna errors, Journal of

840 Atmospheric and Oceanic Technology, 27, 1583-1598, 2010.

Iguchi, T., Hanado, H., Takahashi, N., Kobayashi, S., and Satoh, S.: The dual-frequency precipitation radar for the GPM core satellite, IGARSS 2003. 2003 IEEE International Geoscience and Remote Sensing Symposium. Proceedings (IEEE Cat. No. 03CH37477), 1698-1700,

Iguchi, T., Seto, S., Meneghini, R., Yoshida, N., Awaka, J., Le, M., Chandrasekar, V., and Kubota, T.: GPM/DPR level-2

845 algorithm theoretical basis document, NASA Goddard Space Flight Center, 2010.

Jung, Y., Zhang, G., and Xue, M.: Assimilation of simulated polarimetric radar data for a convective storm using the ensemble Kalman filter. Part I: Observation operators for reflectivity and polarimetric variables, Monthly Weather Review, 136, 2228-2245, 2008.

Le, M. and Chandrasekar, V.: Precipitation type classification method for dual-frequency precipitation radar (DPR) onboard

850 the GPM, IEEE transactions on geoscience and remote sensing, 51, 1784-1790, 2012.

Liebe, H. J., Hufford, G. A., and Manabe, T.: A model for the complex permittivity of water at frequencies below 1 THz, International Journal of Infrared and Millimeter Waves, 12, 659-675, 1991.

Marshall, J. S. and Palmer, W. M. K.: The distribution of raindrops with size, Journal of meteorology, 5, 165-166, 1948.

Mishchenko, M. I.: Calculation of the amplitude matrix for a nonspherical particle in a fixed orientation, Applied optics, 39,

855 1026-1031, 2000.

Mishchenko, M. I.: Electromagnetic scattering by particles and particle groups: an introduction, Cambridge University Press2014.

Mishchenko, M. I. and Travis, L. D.: T-matrix computations of light scattering by large spheroidal particles, Optics communications, 109, 16-21, 1994.

860 Morrison, H. and Milbrandt, J. A.: Parameterization of cloud microphysics based on the prediction of bulk ice particle properties. Part I: Scheme description and idealized tests, Journal of the Atmospheric Sciences, 72, 287-311, 2015.

Oue, M., Tatarevic, A., Kollias, P., Wang, D., Yu, K., and Vogelmann, A. M.: The Cloud-resolving model Radar SIMulator (CR-SIM) Version 3.3: description and applications of a virtual observatory, Geoscientific Model Development, 13, 1975-1998, 2020.

865   Radhakrishna, B.: Raindrop size distribution (DSD) during the passage of tropical cyclone Nivar: effect of measuring principle and wind on DSDs and retrieved rain integral and polarimetric parameters from impact and laser disdrometers, Atmospheric Measurement Techniques, 15, 6705-6722, 2022.

Ryzhkov, A., Pinsky, M., Pokrovsky, A., and Khain, A.: Polarimetric radar observation operator for a cloud model with spectral microphysics, Journal of Applied Meteorology and Climatology, 50, 873-894, 2011.

870   Ryzhkov, A. V.: The impact of beam broadening on the quality of radar polarimetric data, Journal of Atmospheric and Oceanic Technology, 24, 729-744, 2007.

Shen, X., Su, Y., Zhang, H., and Hu, J.: New Version of the CMA-GFS Dynamical Core Based on the Predictor–Corrector Time Integration Scheme, Journal of Meteorological Research, 37, 273-285, 2023.

Skamarock, W. C., Klemp, J. B., Dudhia, J., Gill, D. O., Liu, Z., Berner, J., Wang, W., Powers, J. G., Duda, M. G., and Barker,
875   D. M.: A description of the advanced research WRF version 4, NCAR tech. note ncar/tn-556+ str, 145, 2019.

Thompson, G., Field, P. R., Rasmussen, R. M., and Hall, W. D.: Explicit forecasts of winter precipitation using an improved bulk microphysics scheme. Part II: Implementation of a new snow parameterization, Monthly Weather Review, 136, 5095-5115, 2008.

Thurai, M., Huang, G., Bringi, V., Randeu, W., and Schönhuber, M.: Drop shapes, model comparisons, and calculations of
880   polarimetric radar parameters in rain, Journal of atmospheric and oceanic technology, 24, 1019-1032, 2007.

Van de Hulst, H.: Light scattering by small particles, 1981.

Walters, D., Best, M., Bushell, A., Copsey, D., Edwards, J., Falloon, P., Harris, C., Lock, A., Manners, J., and Morcrette, C.: The Met Office Unified Model global atmosphere 3.0/3.1 and JULES global land 3.0/3.1 configurations, Geoscientific Model Development, 4, 919-941, 2011.

885   Wang, J., Dong, X., Xi, B., and Heymsfield, A. J.: Investigation of liquid cloud microphysical properties of deep convective systems: 1. Parameterization raindrop size distribution and its application for stratiform rain estimation, Journal of Geophysical Research: Atmospheres, 121, 10,739-710,760, 2016.

Wang, S. and Liu, Z.: A radar reflectivity operator with ice-phase hydrometeors for variational data assimilation (version 1.0) and its evaluation with real radar data, Geoscientific Model Development, 12, 4031-4051, 2019.

890   Wang, Z., Bi, L., and Kong, S.: Flexible implementation of the particle shape and internal inhomogeneity in the invariant imbedding T-matrix method, Optics Express, 31, 29427-29439, 2023.

Wolfensberger, D. and Berne, A.: From model to radar variables: a new forward polarimetric radar operator for COSMO, Atmospheric Measurement Techniques, 11, 3883-3916, 2018.

Yang, P., Wendisch, M., Bi, L., Kattawar, G., Mishchenko, M., and Hu, Y.: Dependence of extinction cross-section on incident
895   polarization state and particle orientation, Journal of Quantitative Spectroscopy and Radiative Transfer, 112, 2035-2039, 2011.

Zeng, Y., Blahak, U., and Jerger, D.: An efficient modular volume-scanning radar forward operator for NWP models: description and coupling to the COSMO model, Quarterly Journal of the Royal Meteorological Society, 142, 3234-3256, 2016.

Zeng, Y., Blahak, U., Neuper, M., and Jerger, D.: Radar beam tracing methods based on atmospheric refractive index, Journal of Atmospheric and Oceanic Technology, 31, 2650-2670, 2014.

900 Zhang, G.: Weather radar polarimetry, Crc Press2016.